Earth Syst. Sci. Data, 18, 8865–8901, 2026
https://doi.org/10.5194/essd-18-8865-2026
© Author(s) 2026. This work is distributed under
the Creative Commons Attribution 4.0 License.

Open Access Earth System Science Data

Overview of ParallelClim-WestUS-Daily – high-resolution observed and counterfactual daily climate data for the western United States, 1951–2025

A. Park Williams[1,2,3], John T. Abatzoglou[4], Gavin D. Madakumbura[1,2], Haibo Liu[5], Stefan Rahimi[6], and Christopher Daly[7]

[1]Scripps Institution of Oceanography, University of California, San Diego, La Jolla, CA, USA
[2]Department of Geography, University of California, Los Angeles, CA, USA
[3]Department of Atmospheric and Oceanic Sciences, University of California, Los Angeles, CA, USA
[4]Management of Complex Systems Department, University of California, Merced, CA, USA
[5]Lamont-Doherty Earth Observatory, Columbia University, Palisades, NY, USA
[6]Department of Atmospheric Science, University of Wyoming, Laramie, WY, USA
[7]PRISM Climate Group, Northwest Alliance for Computational Science and Engineering, College of Engineering, Oregon State University, Corvallis, OR, USA

Correspondence: A. Park Williams (p9williams@ucsd.edu)

Received: 22 May 2026 – Discussion started: 17 July 2026
Revised: 13 November 2026 – Accepted: 17 November 2026 – Published: 25 November 2026

Abstract. Extreme climate events and trends commonly elicit curiosity as to the role of anthropogenic climate change. In the western United States (US), severe droughts and heatwaves over the first quarter of the 21st century have strained water-management, agricultural, and ecological systems while also putting humans at risk from wildfires and hydrological hazards. Understanding whether and how climate change has promoted or intensified these processes requires estimating anthropogenic effects on a wide range of climate variables, including background mean conditions, higher-frequency variances, and how these changes have been distributed intra-annually and spatially. Here we introduce ParallelClim-WestUS-Daily, a new dataset of observed daily, high-resolution (∼4 km) gridded climate data for the western US from 1951–2025 as well as a parallel, counterfactual realization of the observed sequence of climate but excluding anthropogenic changes in background mean climate and daily variances. Our dataset includes eight surface variables commonly used in hydrological, vegetation, and wildfire modeling: daily precipitation total, daily maximum and minimum temperature, and daily means of vapor pressure, wind speed, downwelling shortwave and longwave radiation, and surface pressure. Anthropogenic climate change is estimated as the weighted mean change among 24 climate models relative to the second half of the 19th century according to the CMIP6 Historical experiment through 2014, extended with SSP2-4.5 for 2015–2025. Model weightings are based on agreement with global surface temperature trends, limiting the influence of models with likely unrealistic climate sensitivities to greenhouse-gas forcing. The ParallelClim-WestUS-Daily dataset will allow new opportunities to explore effects of anthropogenic climate change on western US hydroclimate and complex hydroclimatic impacts such as soil moisture, snowpack, streamflow, vegetation productivity, and wildfire. The ParallelClim-WestUS-Daily dataset is available at https://doi.org/10.5281/zenodo.19636838 (Williams, 2026c) for the observed climate and https://doi.org/10.5281/zenodo.20261472 (Williams, 2026b) for the counterfactual climate.

Published by Copernicus Publications.

1 Introduction

As the globe warms due to an intensifying anthropogenic greenhouse effect, some land areas are projected to become wetter on average, others drier, and most will experience increasingly variable hydroclimatic swings (Giorgi et al., 2011; Pendergrass et al., 2017; Pfahl et al., 2017; Cook et al., 2020; Swain et al., 2025). As hydroclimatic normals and variances change, it will be increasingly important to understand how anthropogenic forcing drives not only observed trends and extreme hydroclimate events, but also their complex impacts on hydrology, ecosystems, and wildfire.

In the western United States (US), the first quarter of the 21st century was likely as dry or drier on average than any similar-length period in at least 1200 years. This resulted from a shift toward lower precipitation around 2000 combined with a century-long warming trend that enhanced atmospheric evaporative demand (Williams et al., 2020, 2022b) and led to widespread hydrological impacts, including declines in snowpack, streamflow, reservoir storage, and groundwater (Faunt et al., 2016; Mote et al., 2018; Rodell et al., 2018; Xiao et al., 2018; Musselman et al., 2021; Williams et al., 2022a; Gottlieb and Mankin, 2024). These changes led to follow-on impacts such as shifts in agricultural activities (Howitt et al., 2014), tree mortality (Williams et al., 2013; Hicke et al., 2016; Berner et al., 2017; Anderegg et al., 2019), increased forest-fire sizes and severities (Juang et al., 2022; Parks et al., 2025; Hung and Williams, 2026), and reduced net primary productivity (Schwalm et al., 2012). Studies have shown that these significant hydroclimatic shifts in the western US over the last several decades were promoted by a combination of anthropogenic climate trends and natural variability, in part driven by a La Niña-like trend in the tropical Pacific (Lehner et al., 2018; Seager et al., 2023; Pillai et al., 2026).

Various methods exist to use climate models to quantitatively attribute observed climate trends or events to anthropogenic forcing versus natural variability (National Academies of Sciences, Engineering, and Medicine, 2016). A traditional approach is to identify an observed climate condition (e.g., a heat wave) and assess how anthropogenic forcing affected its probability by comparing simulations driven by observed historical forcings that include anthropogenic forcing to a counterfactual ensemble forced solely by natural drivers (Hannart et al., 2016). However, climate models may not adequately simulate the specific process of interest. For example, they appear to under-represent prolonged droughts (Ault et al., 2014; Noyelle et al., 2026), have spatiotemporal biases in the El Niño-Southern Oscillation (ENSO) (Bellenger et al., 2014; Dieppois et al., 2021; Planton et al., 2021), and mis-represent heatwave characteristics (Hirsch et al., 2021). Additionally, global climate models do not reliably simulate many hydroclimatic impacts like soil moisture, snowpack, streamflow, ecosystem dynamics, or wildfire, particularly at the fine spatial scales of individual watersheds.

For many hydroclimatic impacts (e.g., streamflow), offline modeling – where climate model outputs force a separate impact model – may be necessary to realistically simulate the relevant processes. Offline modeling often requires multiple climate variables (e.g., precipitation, temperature, humidity, wind speed, and radiation) and may necessitate long simulations (decades or centuries) if the impact of interest depends on slow processes like tree growth or more complex ecosystem dynamics such as forest disturbance, competition, and succession. Furthermore, offline modeling can be highly computationally demanding. At the time of writing, running version 5 of the Noah-MP land surface model (He et al., 2023) at 4 km spatial resolution with hourly output across the western US, with complex representations of groundwater, vegetation, and snow, takes about half a day per simulated year on one 128-core AMD EPYC 7763 node of a supercomputer. For these reasons, it is often infeasible to take the traditional paired-large-ensemble approach for climate-change attributions of observed hydroclimatic impacts, particularly at fine spatial scales for ecosystem and hydrologic modeling.

Consequently, alternative methods have been developed to apply the counterfactual framework directly to climate observations. This allows the observed, factual climate record to be compared directly to a counterfactual realization of those same observations, as can outputs from offline simulations forced by factual and counterfactual records. Therefore, instead of large ensemble-based exploration of full probability distributions, these methods allow for comparing the magnitudes of observed, factual events (including trends) and their counterfactual counterparts, under the assumption that the exact same sequence of meteorological variability occurred in the counterfactual world.

One method for producing counterfactual observations is dynamical adjustment, where a counterfactual record is generated by statistically removing climate variations unaccounted for by variations in large-scale atmospheric pressure patterns (dynamics) (Deser et al., 2016). A limitation is its simplifying assumptions: atmospheric dynamics (wind) and thermodynamics (heat) are independent, anthropogenic climate change does not affect dynamics, and thermodynamically-driven trends are entirely externally forced. However, anthropogenic forcing is expected to drive poleward shifts in large-scale atmospheric circulation, including the descending branch of the Hadley cell, the jet stream, and synoptic features such as atmospheric rivers, and these changes may already be underway (Marvel and Bonfils, 2013; Payne and Magnusdottir, 2015; Li and Ding, 2024). Furthermore, isolating the dynamical component requires fitting statistical models between the climate variable and atmospheric pressure fields. Results are thus sensitive to observational or reanalysis data quality, as well as methodological choices like spatial domain, sample size, and statistical modeling method. To date, no efforts have used dynamical adjustment to produce a large database of high-resolution daily climate grids across a broad domain like the western

US for a wide range of variables, thus limiting the usefulness of the dynamical adjustment technique to explore complex processes requiring offline modeling.

Another counterfactual method was used for the Attributing Climate Impacts (ATTRICI) counterfactual dataset (Mengel et al., 2021), which provides global daily 0.5° resolution climate variables for 1901–2019. ATTRICI quantifies the relationship between background mean climate and a smoothed global mean temperature record, then statistically removes the correlation-inferred effect of global temperature changes from observed climate. This approximates a counterfactual world unaffected by low-frequency global temperature changes since 1901. Its strengths are being computationally straightforward and globally applicable. Drawbacks include the implicit assumption that all observed low-frequency global temperature variations are anthropogenically forced, negating natural variations like ocean oscillations. Additionally, its spatial resolution is too coarse for many offline hydrological applications. Its global scope also necessitates using reanalysis products rather than true observations, and prior to 1979, the reliability of these products changes considerably due to shifting observational data density.

An increasingly common alternative is the "remove-the-modeled-trend" (RTMT) approach, which simply removes anthropogenically forced trends as simulated by climate models from observations. For example, Abatzoglou and Williams (2016) approximated anthropogenic trends in temperature and humidity as the multi-model mean low-pass filtered changes simulated by 27 CMIP5 models (Taylor et al., 2012). Counterfactual versions were calculated by subtracting these trends from observations to evaluate how anthropogenic effects altered fuel dryness metrics strongly related to annual area burned in western US forests. Diffenbaugh and Burke (2019) used a similar approach for temperature records to assess anthropogenic warming effects on global economic inequality. Williams et al. (2020) evaluated counterfactual monthly gridded soil moisture at 0.25° resolution across North America by removing CMIP5-simulated trends in temperature, humidity, and precipitation, later updated by Williams et al. (2022b) with the 6th phase of the Coupled Model Intercomparison Project (CMIP6) (Eyring et al., 2016). These or similar counterfactual records have been used in a number of subsequent hydrological and ecological assessments (Stephens et al., 2023; Williams et al., 2024b; Dannenberg et al., 2025; Williams and Abatzoglou, 2025). The global dataset TerraClimate v1.1 (Abatzoglou et al., 2018) also recently added counterfactual monthly 4 km precipitation, temperature, vapor pressure, wind speed, and solar radiation covering 1950–2025, though it relies entirely on reanalysis climate.

A weakness of the RTMT approach to date is the assumption that the anthropogenic effect is simply a monotonic forcing on the background mean climate, with no effect on higher-frequency variability. Furthermore, by defining the anthropogenic forcing as the change in background mean state since 1901, most of these efforts ignore any anthropogenic forcing prior to 1901, though these effects are believed to be relatively small compared to those of the 20th and 21st centuries (Eyring et al., 2023).

Despite its limitations, the RTMT method is computationally efficient, allowing for easy real-time updates and application to the wide range of variables needed to force offline models of hydroclimatic impacts (e.g., hydrological, vegetation, or wildfire models). It does not require high-quality atmospheric pressure fields, unlike dynamical adjustment, and thus is not subject to changes in the quality of reanalysis pressure data. Additionally, while all published RTMT datasets that we are aware of only remove anthropogenic trends in monthly means, RTMT methods should not be limited to removing background mean trends; they can also be applied to produce counterfactual realizations of daily data from which modeled trends in daily variance are removed. Anthropogenic forcing is understood to change not just background mean climate but also higher-frequency variations such as precipitation frequencies and extremes (Pfahl et al., 2017; Zhang et al., 2021), but to our knowledge effects on climate variability have not been accounted for in prior RTMT efforts. Accounting for anthropogenically forced changes in daily variances would be particularly helpful for offline simulation of processes that respond non-linearly to daily climate variability, such as snowpack and wildfire.

Here we present ParallelClim-WestUS-Daily, a database of observed and counterfactual daily surface climate for the western US at 1/24° resolution covering 1951–2025. The daily variables represented are precipitation total (prec, mm), maximum temperature (t_{max}, °C), minimum temperature (t_{min}, °C), mean vapor pressure (ea, hPa), mean 2 m wind speed (wind, $m\,s^{-1}$), mean downwelling solar radiation at the surface (solar, $W\,m^{-2}$), mean downwelling longwave radiation at the surface (longwave, $W\,m^{-2}$), and surface pressure (psfc, hPa). The fine spatial and temporal resolutions, alongside the breadth of variables, enable straightforward use in an offline modeling framework. Anthropogenic climate trends are assessed using outputs from 24 CMIP6 models, with the multi-model mean weighted by agreement with observed global temperature trends to reduce the effect of models with unrealistically high sensitivity to greenhouse-gas forcing (Hausfather et al., 2022). An advance of the counterfactual component of ParallelClim-WestUS-Daily is that, beyond removing anthropogenic trends in background means, we also remove anthropogenic changes in distributions of daily departures from those means. This paper details the methods underlying ParallelClim-WestUS-Daily, a parallel pair of observed and counterfactual datasets designed to enable long-term (75-year) assessments of western US hydroclimatic events and their anthropogenic climate change contributions.

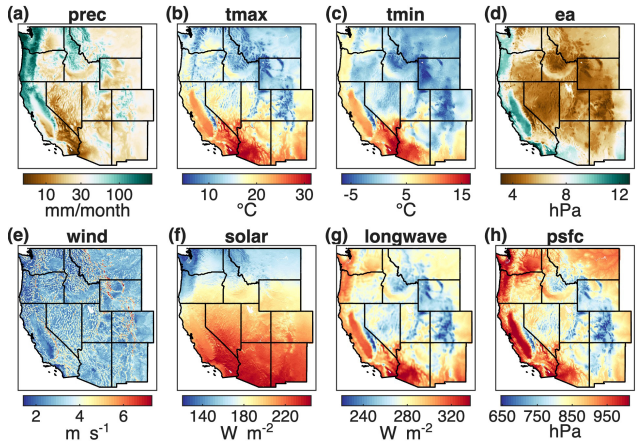

Figure 1. Observed climatological means (1951–2025) of the eight variables: **(a)** precipitation total (prec), **(b)** daily maximum temperature (t_{max}), **(c)** daily minimum temperature (t_{min}), **(d)** vapor pressure (ea), **(e)** wind speed 2 m above the surface (wind), **(f)** downwelling solar radiation (solar), **(g)** downwelling longwave radiation (longwave), and surface pressure (psfc).

2 Data sources and methods

We produce daily grids of climate for the 75-year period from 1 January 1951 to 31 December 2025 at a geographic resolution of 1/24° (∼4 km) across the western US domain mapped in Fig. 1. We define the western US as the 11 westernmost states in the coterminous US (Arizona, California, Colorado, Idaho, Montana, New Mexico, Nevada, Oregon, Utah, Washington, and Wyoming).

2.1 Observed climate

Maps of the observed long-term (1951–2025) climatologies for the eight variables are shown in Fig. 1.

Daily prec, t_{max}, and t_{min} data come from the 1/24° nClimGrid-daily dataset produced by the National Oceanic and Atmospheric Administration (NOAA), which covers 1951–present (Durre et al., 2022). We use the 1/24° latitude/-longitude coordinates of the nClimGrid-daily dataset to define the resolution and grid-cell central locations of our data.

Daily ea data are calculated from the daily 1/24° gridded PRISM AN81d dataset, produced by the PRISM group at Oregon State University, which covers 1981–present (Daly et al., 2021). While PRISM does not provide ea grids directly, they provide daily mean dew point (tdew, °C). We estimate ea ($ea_{t_{dew}}$) from tdew using the WMO (2008) Clausius Clapeyron formulation:

$$ea_{t_{dew}} = 6.112e^{\left(\frac{17.62 \cdot t_{dew}}{t_{dew}+243.12}\right)}. \quad (1)$$

Given the exponential response of $ea_{t_{dew}}$ to tdew and the fact that tdew is a daily mean value, $ea_{t_{dew}}$ is likely to be consistently lower than true ea. Because PRISM also provides daily grids of t_{max} and t_{min} as well as their associated vapor-pressure deficits (vpd_{max} and vpd_{min}, respectively; hPa), we also calculate ea at t_{max} and t_{min} ($ea_{t_{max}}$ and $ea_{t_{min}}$, respectively). To do this, we first calculate daily maximum and minimum saturation vapor pressure (es_{max} and es_{min}, respectively; hPa):

$$es_{max} = 6.112e^{\left(\frac{17.62 \cdot t_{max}}{t_{max}+243.12}\right)} \quad (2)$$

and

$$es_{min} = 6.112e^{\left(\frac{17.62 \cdot t_{min}}{t_{min}+243.12}\right)}. \quad (3)$$

We then calculate $ea_{t_{max}}$ and $ea_{t_{min}}$ as:

$$ea_{t_{max}} = es_{max} - vpd_{max} \quad (4)$$

and

$$ea_{t_{min}} = es_{min} - vpd_{min}. \quad (5)$$

Finally, we estimate daily mean ea as the average of $ea_{t_{dew}}$, $ea_{t_{max}}$, and $ea_{t_{min}}$:

$$ea = \left(ea_{t_{dew}} + ea_{t_{max}} + ea_{t_{min}}\right)/3. \quad (6)$$

However, grid-cell locations of the 1/24° PRISM data are offset from those of our dataset's map by half of a grid width (1/48°) in the zonal and meridional directions. We address this by, for each 1/24° grid in our dataset's map, averaging across the values of all (usually four) overlapping PRISM grid cells. We then bias correct these spatially smoothed maps using monthly data from the high-resolution (1/120°) version of PRISM (AN81n). For each 1/24° grid cell in our western US domain, each month from 1981–2025, and each PRISM variable (t_{dew}, t_{max}, t_{min}, vpd_{max}, and vpd_{min}), we calculate the true monthly mean as the average of all (usually 16) 1/120° gridded values within. We then additively adjust the daily 1/24° maps such that, for each month, each grid cell's daily values average to equal the true monthly mean calculated from 1/120° data.

Because the PRISM daily product only goes back to 1981, we extend PRISM ea back to 1951 using a calibrated version of the dynamically-downscaled ERA5 reanalysis (Hersbach et al., 2020) for the western US produced by Rahimi et al. (2022). The Rahimi et al. dataset has a 9 km spatial resolution and covers September 1950–March 2025. We use the Rahimi et al. daily outputs of mean specific humidity (q, $m^3\ m^{-3}$) and surface pressure (psfc, hPa) to calculate ea:

$$ea = psfc \cdot q/(0.622 + 0.378 \cdot q). \quad (7)$$

We bilinearly interpolate the 9 km grids of ea to 1/24° resolution and use quantile mapping to calibrate such that, for each grid cell and each of the 12 months, the distributions of daily ea estimated from Rahimi et al. match those from PRISM during 1981–2020.

While observations are ideal, the dynamically downscaled ERA5 data from Rahimi et al. (2022) are preferred over the original ERA5 data due in part to higher spatial resolution (9 km versus 30 km) to provide a more realistic representation of the effects of topography and surface-atmosphere coupling. Rahimi et al. (2022) performed a sequence of ~ 20 sensitivity tests to identify optimal model options (e.g., convective schemes) and grid options (e.g., nudging) to minimize biases in western US hydroclimate (e.g., snow, temperature, and precipitation) and winds, showing generally reduced biases compared to the original ERA5 (e.g., in California, improved surface winds and relative humidity during offshore wind events at surface stations compared to ERA5). Even with the optimal model options, however, downscaled 9 km ERA5 was still shown to underpredict the diurnal temperature range, overpredict summertime precipitation across the Desert Southwest, and overestimate t_{max} at the highest elevations.

Because we obtain ea and temperature from different sources, there may be rare cases when daily mean ea exceeds the daily mean saturation vapor pressure (es; hPa) implied by the temperature data. We do not adjust ea, t_{max}, or t_{min} to correct for this, as the nonlinear nature of the Clausius Clapeyron equation dictates that any calculation of daily mean ea or es from the temporal means of tdew and temperature are merely estimates because ea and es relate nonlinearly to tdew and temperature (He et al., 2025). We thus note that users of this dataset who are performing calculations involving ea and es may wish to adjust ea to avoid cases in which ea exceeds their estimates of es.

For wind, we use the WTK-LED dynamically-downscaled ERA5 wind reanalysis as the primary dataset, which has 4 km geographic resolution and covers 2001–2020 (Draxl et al., 2024) and has been shown to be skillful across the western US (Peco et al., 2026). We prioritize the WTK-LED wind data over those from Rahimi et al. (2022) because of WTK-LED's higher geographic resolution and because the relatively deep wind-specific validation documented by Peko et al. shows major improvements relative to ERA5. We calculate daily mean wind speed from hourly means at 10 m above the surface and interpolate to our $1/24°$ grid using nearest neighbor. We adjust the 10 m wind speed values to represent those expected at a 2 m height by multiplying by 0.748 ($4.87/\ln(67.8 \cdot 10\,\text{m} - 5.42)$) following the FAO56 Penman-Monteith methodology (Allen et al., 1998). We extend this dataset back to 1951 and forward through March 2025 using the daily mean 10 m wind speed from the Rahimi et al. (2022) 9 km reanalysis, bilinearly interpolated to $1/24°$ resolution, and multiplied by 0.748. Because this dataset ends in March 2025, we extend through December 2025 using 10 m daily mean wind speed from GridMET, which covers 1979–present (Abatzoglou, 2013). We bias correct the Rahimi et al. (2022) and GridMET data using quantile mapping such that each dataset's daily wind speed distribution matches that of WTK-LED during 2001–2020 for each grid cell and each of the 12 months.

For solar, we use the newly available, observation-based daily $1/24°$ dataset from PRISM AN81d as the primary dataset (Rupp et al., 2022), which covers 1981–present. As is the case for ea, this dataset is geographically offset by $1/48°$ from our grid, so we follow the same correction approach as for ea to ensure that monthly means on our $1/24°$ grid match those calculated from the high-resolution $1/120°$ PRISM AN81n dataset. The solar dataset we use from PRISM accounts for the effect of topographic slope and aspect on incident downward solar radiation at the surface. We extend solar back to 1951 using daily mean solar from the Rahimi et al. (2022) 9 km reanalysis, downscaled to $1/24°$, and bias corrected using quantile mapping to match PRISM distributions during 1981–2020.

For longwave and psfc, we use the Rahimi et al. (2022) 9 km reanalysis, interpolated to $1/24°$ resolution, as the primary source for 1951 through March 2025. For April–December 2025, we use the hourly climate forcing dataset produced for the second phase of the North American Land Data Assimilation System (NLDAS2), which has $1/8°$ geographic resolution covers 1979–present (Xia et al., 2012). We calculate daily means, bilinearly interpolate to $1/24°$ resolution, and bias correct using quantile mapping to match Rahimi et al. distributions during 1981–2020.

Although quantile mapping enforces matching distributions of daily values at the grid-cell level, there is no guarantee that a quantile mapped dataset will share other properties with its target dataset such as trends, temporal covariations, or autocorrelation properties. In Fig. A1, we plot annual time series of regionally averaged climate and show generally good agreement among datasets for each of the five variables composed of multiple underlying datasets (ea, wind, solar, longwave, psfc). Interannual covariability is generally strong among datasets during periods of overlap and relative differences are generally well below 5 %. We thus do not expect use of this dataset to be limited by unrealistic temporal discontinuities caused by transitions between datasets.

2.2 CMIP6-detrended climate

Here we produce a counterfactual version of the observed climate dataset described above, but where anthropogenic trends in background means and daily variances are removed such that the climatology is consistent with what would have been expected in the second half of the 1800s. Below, we describe the approach to selecting CMIP6 models and determining weightings for multi-model mean calculations, followed by descriptions of how we estimate anthropogenic changes in background means as well as changes in daily variations about those means.

2.2.1 CMIP6 models

We estimate anthropogenic climate change to be represented by the CMIP6 24-model weighted mean trends in background means and the variances of daily departures from those means. See Table A1 for a list of the 24 models considered and Sect. 2.2.2 for a description of the model weighting. For 1850–2014 we use simulations from the CMIP6 Historical scenario and for 2015–2025 we use simulations from the Shared Socioeconomic Pathway 2-4.5 (SSP2-4.5) (Eyring et al., 2016). The SSP2-4.5 represents a commonly used middle-of-the-road future emissions trajectory. Notably, the degree of anthropogenic climate forcing in this scenario is not markedly different from that of other CMIP6 SSP scenarios during the 2015–2025 period of overlap with our dataset's observational period (O'Neill et al., 2016). According to data from Meinshausen et al. (2020), the global mean CO_2 concentration in 2025 under SSP2-4.5 is approximately 429 parts per million (ppm), which is within approximately 1 % of that assumed under the other SSPs, and well aligned with the observed value of 427 ppm (WMO, 2026). We consider anthropogenic climate trends to be departures in the 24-model mean climate conditions from an 1851–1900 baseline.

The 24 CMIP6 models considered are selected mainly based on data availability, with the primary criterion being that daily outputs are available via the CMIP6 data portal hosted by the Earth System Grid Federation (Williams et al., 2016; https://aims2.llnl.gov/search/cmip6/, last access: 15 April 2026) for prec, temperature, ea, wind, solar, longwave, and psfc for at least one continuous ensemble member under the Historical and SSP2-4.5 scenarios. For temperature, most models provide t_{max} and t_{min} but for models missing these variables we use mean temperature (tave; °C) to estimate t_{max} and t_{min} based on the multi-model mean of offsets between t_{max}, t_{min}, and tave derived, for each of the 12 months, from the models that provide data for all three variables. At the time of our acquisition of CMIP6 data, 28 models provide daily outputs for the Historical and SSP2-4.5 scenarios for the required variables. However, it is preferable that models also provide *monthly* mean data for more than one realization of Historical and SSP2-4.5 climate. This is because anthropogenic climate change is dominated by changes in background mean conditions, as opposed to changes to higher-frequency variability, and thus a model's true anthropogenic change in climate is best represented by the average of multiple realizations. Of the 28 models with adequate daily data, we exclude four (CMCC-ESM2, GFDL-CM4, IITM-ESM, KIOST-ESM) because they provide monthly outputs for only a single realization. One additional model is represented by a single realization with monthly outputs (INM-CM4-8) but this model is included because we find that this model simulates a relatively realistic mean western US climatology. The CMCC-CM2-SR5 also has only one realization available for some variables but we consider this model because it provides three historical realizations for prec and tave, variables that are particularly impactful for western US hydroclimate. See Table 1 for the number of ensemble members with monthly data available for each model.

Because ea is not a standard CMIP6 output, we calculate daily and monthly means of CMIP6 ea from q and psfc using Eq. (7). For some CMIP6 ensemble members, outputs are not available for ea or psfc but are available for relative humidity (RH, %) and temperature. We estimate ea for these ensemble members as $\mathrm{es} \cdot \mathrm{RH}/100$, where es is estimated from t_{max} and t_{min} (or from tave when t_{max} and t_{min} are lacking). Additionally, some ensemble members lack outputs for psfc. In these cases we estimate psfc from mean sea level pressure (psl; hPa), tave, and elevation (h; m a.s.l.) following NOAA (1976):

$$\mathrm{psfc} = \mathrm{psl}\left(1 - \frac{L \cdot h}{\mathrm{tave} + 273.15 + L \cdot h}\right)^{\frac{g \cdot M}{R \cdot L}}, \tag{8}$$

where L is the standard temperature lapse rate ($0.0065\,^{\circ}\mathrm{C\,m^{-1}}$), g is the gravitational acceleration ($9.80665\,\mathrm{m\,s^{-2}}$), M is the molar mass of dry air ($0.0289644\,\mathrm{kg\,mol^{-1}}$), and R is the universal gas constant ($8.31432\,\mathrm{J\,mol^{-1}\,K^{-1}}$).

All monthly and daily outputs of CMIP6 climate are regridded to a common 1° geographic resolution using bilinear interpolation. Notably, for solar and longwave, daily outputs from the Historical simulations from the ACCESS-CM2 and ACCESS-ESM1-5 models do not begin until 1950, so these models are not used to estimate anthropogenic effects on daily variances for these variables. Similarly, daily outputs for wind are not available for CNRM-CM6-1 and CNRM-ESM2-1 simulations under the SSP2-4.5 scenario, so those models do not contribute to our assessment of anthropogenic effects on daily wind variability.

2.2.2 CMIP6 model weighting

In our use of CMIP6 multi-model means to represent anthropogenic climate change, we apply the ClimWIP method to weight each model's contribution based on model independence and performance (Knutti et al., 2017a; Sanderson et al., 2017; Lorenz et al., 2018; Brunner et al., 2020; Merrifield et al., 2020). The purpose of ClimWIP is to reduce risk of incorporating information from models unlikely to reliably simulate the process of interest while also not placing disproportionate weight on groups of closely related models (Sanderson et al., 2015; Knutti et al., 2017b). The weighting ($\boldsymbol{w}$) is calculated as

$$\boldsymbol{w}_i = \boldsymbol{P}_i \boldsymbol{I}_i, \tag{9}$$

where $\boldsymbol{P}$ is a performance metric and $\boldsymbol{I}$ is an independence metric for each model (m_i). The $\boldsymbol{P}$ metric is calculated as

$$\boldsymbol{P}_i = e^{-\left(\frac{D_i}{\sigma_D}\right)^2}, \tag{10}$$

Table 1. CMIP6 models used to quantify anthropogenic climate trends. For each model and climate variable, three values are provided. First value: number of Historical simulations considered. Second value: number of SSP2-4.5 simulations considered. Third value: number of combinations of Historical and SSP2-4.5 simulations used to estimate trends in background monthly means (see Sect. 2.2.2). For the five models without t_{max} and t_{min} data, we estimated t_{max} and t_{min} from tave by applying the mean offsets between t_{max}, t_{min}, and tave from the 19 models with data for all three variables.

	prec	t_{max}	t_{min}	ea	wind	solar	longwave	psfc
ACCESS-CM2	5/5/10	5/5/10	5/5/10	5/5/10	3/3/3	3/3/9	3/3/9	5/5/10
ACCESS-ESM1-5	40/40/40	40/40/40	40/40/40	40/40/40	19/19/19	18/18/18	19/19/19	40/40/40
CESM2	7/7/10	0/0/0	0/0/0	7/6/10	7/7/10	7/7/10	7/7/10	7/6/10
CESM2-WACCM	3/3/10	0/0/0	0/0/0	3/4/10	3/3/10	3/3/10	3/3/10	3/4/10
CMCC-CM2-SR5	3/3/3	0/0/0	0/0/0	3/1/3	3/3/3	3/3/3	3/3/3	3/1/3
CNRM-CM6-1	6/6/10	6/6/10	6/6/10	6/6/10	6/6/10	6/6/10	6/6/10	6/6/10
CNRM-ESM2-1	9/9/10	9/9/10	9/9/10	9/9/10	9/9/10	9/9/10	9/9/10	9/9/10
CanESM5	50/50/50	50/50/50	50/50/50	50/50/50	50/50/50	50/50/50	50/50/50	50/50/50
EC-Earth3	21/21/21	21/21/21	22/22/22	21/21/21	15/15/15	16/16/16	16/16/16	18/18/18
EC-Earth3-Veg	8/8/10	8/8/10	8/8/10	6/6/9	8/8/9	8/8/9	8/8/9	7/6/9
FGOALS-g3	6/6/10	6/6/10	6/6/10	6/4/10	6/6/10	6/6/10	6/6/10	6/4/10
GFDL-ESM4	3/3/9	3/3/9	3/3/9	3/3/9	1/1/1	2/2/2	3/3/6	3/3/9
HadGEM3-GC31-LL	5/5/5	5/5/5	5/5/5	5/1/5	5/5/5	5/5/5	5/5/5	5/1/5
INM-CM4-8	1/1/1	1/1/1	1/1/1	1/1/1	1/1/1	1/1/1	1/1/1	1/1/1
INM-CM5-0	10/10/10	10/10/10	10/10/10	10/1/10	10/10/10	10/10/10	10/10/10	10/1/10
KACE-1-0-G	3/3/9	3/3/9	3/3/9	3/3/9	3/3/9	3/3/9	3/3/9	3/3/9
MIROC-ES2L	30/30/30	30/30/30	30/30/30	30/30/30	30/30/30	30/30/30	30/30/30	30/30/30
MIROC6	50/50/50	33/33/33	33/33/33	33/33/33	8/8/10	8/8/10	8/8/10	49/49/49
MPI-ESM1-2-HR	9/9/10	9/9/10	9/9/10	9/2/10	9/9/10	9/9/10	9/9/10	9/2/10
MPI-ESM1-2-LR	30/30/30	30/30/30	30/30/30	30/30/30	30/30/30	30/30/30	30/30/30	30/30/30
MRI-ESM2-0	7/7/10	7/7/10	7/7/10	8/2/10	7/7/7	7/7/7	7/7/7	10/1/10
NorESM2-LM	3/3/9	0/0/0	0/0/0	3/3/9	3/3/9	3/3/9	3/3/9	3/3/9
NorESM2-MM	3/3/6	0/0/0	0/0/0	3/2/6	3/3/6	3/3/6	3/3/6	3/2/6
UKESM1-0-LL	13/13/13	7/7/10	7/7/10	13/13/13	7/7/10	13/13/13	13/13/13	13/13/13

where $\boldsymbol{D}$ is a vector of each model's normalized difference from an observational target used to assess model performance and σ_D is a difference shape parameter, which we define to be 0.42, as described below. For our observational target variable, we use the least-squares linear change in global mean surface temperature from 1961–2025 as represented by three observational datasets. These datasets are from NOAA, the National Aeronautics and Space Administration's Goddard Institute for Space Studies (NASA GISS), and Berkeley Earth. Their respective changes in global mean surface temperature from 1961–2025 are +1.142, +1.184, and +1.223 °C. For each model, we calculate the change in global mean surface air temperature (tas) from 1961–2025 for all available ensemble members for which monthly tas is available from the Historical and SSP2-4.5 experiments (see Table 2 for number of ensemble members per model). For each model, i, and ensemble member, we calculate the absolute difference from each of the three, k, observed trend values. For each model and observational value, the performance metric, d_{ik}, is calculated as the average absolute difference among ensemble members and then for each model, $d_i{}'$ is calculated as the root mean of squared d_{ik} values. Finally, $\boldsymbol{D}_i$ is calculated by dividing each model's $d_i{}'$ value by the all-model mean d'. Table 2 lists each model's ensemble-mean linear temperature change, the difference between this value and the mean of the three observational values, as well as the normalized values of $\boldsymbol{D}$.

Our choice to use the global temperature trend as the basis of our observation-constrained weighting reflects the high likelihood that several CMIP6 models simulate an unrealistically high climate sensitivity (warming per doubling of CO_2) that is unsupported by observations, theory, and paleoevidence (Knutti et al., 2017b; Zhu et al., 2020; Hausfather et al., 2022). Indeed, weighting models by their performance at simulating observed temperature trends leads to lower inferred rates of past and future anthropogenic warming (Brunner et al., 2020; Tokarska et al., 2020; Hausfather et al., 2022). There are many ways to assess model agreement with observed trends (e.g., global mean or spatially explicit, annual or seasonal). Our choice to weight based on agreement with the observed global trend over 1961–2025 reflects our prioritization of simplicity and interpretability. Weighting models based on reproduction of more nuanced characteristics of the observed climate system would risk overfitting our impression of anthropogenic trends to the observed record. Our choice of the 1961–2025 period reflects that, ac-

cording to observations and most models, the vast majority of anthropogenic warming has occurred during this time following a multi-decade period of stable or cooling temperatures in the mid-19th century. Thus, focusing on 1961–2025 allows us to reasonably characterize warming trends as linear while still capturing most of the anthropogenic warming to date.

The independence metric, $\boldsymbol{I}$, is calculated as

$$\boldsymbol{I}_i = 1/\left(1+\sum_{i\neq j}^{M} e^{-\left(\frac{\mathbf{S}_{ij}}{\sigma_S}\right)^2}\right), \tag{11}$$

where $\mathbf{S}_{ij}$ is a matrix quantifying the similarity between all pairs of models, m_i and m_j ($i \neq j$), and σ_S is a similarity shape parameter, which we define to be 0.20 (described below). The goal in calculating the $\mathbf{S}$ matrix is to identify models with shared structural similarities such as offsets or spatial patterns in mean climate relative to other models, which would be interpreted as indicative of shared model components or parameterizations. Following Merrifield et al. (2020) and Brunner et al. (2020), we quantify similarity based on inter-model agreement on maps of climatological mean tas and atmospheric pressure and sea level (psl). For each model we calculate global maps of long-term mean tas and psl for the period 1951–2000 using all ensemble members for which monthly mean data are available from the Historical scenario and then average across ensemble members. All maps are nearest-neighbor interpolated to a common 1° geographic grid. For each variable, v (tas and psl), a 24×24 similarity matrix, $\mathbf{s}_v$, is calculated as the square root of area-weighted mean squared difference between all possible pairs of models:

$$\mathbf{s}_{vij} = \sqrt{\frac{\sum_l^L W_l\left(v_{il}-v_{jl}\right)^2}{\sum_l^L W_l}}, \tag{12}$$

where W_l is the cosine of the latitude of each of the L grid cells in maps v_i and v_j. Diagonals in each similarity matrix (where $i = j$) are assigned zeros and we calculate a normalized version of each similarity matrix ($\mathbf{s}_v{}'$) by dividing by the mean of all values. The final similarity matrix, $\mathbf{S}$, is then calculated by averaging the two $\mathbf{s}_v{}'$ matrices and again normalizing by dividing by the mean. See Table 2 for normalized values of $\boldsymbol{I}$.

The shape parameters for performance and similarity, σ_D and σ_S, respectively, act to modulate the effects of $\boldsymbol{D}$ and $\mathbf{S}$. Small σ_D values (values much smaller than the mean of $\boldsymbol{D}$) cause performance weightings, $\boldsymbol{P}$, to be skewed heavily toward the models with the smallest values of $\boldsymbol{D}$ (e.g., strongest agreement with observed temperature trend). Larger σ_D causes performance weightings to be more evenly distributed among models. The effect of the similarity parameter, σ_S, is generally more subtle than that of σ_D. When σ_S is very low, this causes the independence weighting, $\boldsymbol{I}$, to converge toward one among models for which $\mathbf{S}$ (model uniqueness) is much larger than σ_S, leading to more evenly distributed values of $\boldsymbol{I}$. On the other hand, if σ_S is much higher than most or all values of $\mathbf{S}$, this causes values of $\boldsymbol{I}$ to converge toward 0.5, again leading to more evenly distributed independence weightings.

To determine appropriate values of σ_D and σ_S we use the "perfect-model" scheme described by Knutti et al. (2017a) and Brunner et al. (2020). Briefly, each of the 24 models are treated, one at a time, as if its ensemble-mean temperature trend from 1961–2025 is the true trend, and the remaining 23 models are used to produce a multi-model weighted distribution of trends where weightings are calculated following the methods described above. For each withheld model, this is done 2500 times, each time with a unique combination of potential σ_D and σ_S values. For both parameters, 50 potential values are tested, evenly spaced from 0.2 to 2.0. For each of the 2500 pairs of values, it is tested whether the model-weighting scheme produces a reasonable distribution of temperature-trend estimates. Specifically, we first develop a weighted cumulative distribution (CDF) function of the 23 modeled trends and test whether the "true" trend from the withheld model falls above the 10th percentile and below the 90th percentile (inner 80 % range) within the weighted CDF. After doing this for all withheld models, if $\geq 80\,\%$ of the 24 "true" temperature trends fall within the inner 80% range for a given pair of σ_D and σ_S values, that pair of values is determined capable of producing reasonable weighted trend distributions. Of all reasonable pairs of σ_D and σ_S values, we select the pair with the smallest sum, following Brunner et al. (2020). We find these values are 0.42 for σ_D and 0.20 for σ_S.

The final model weightings based on $\boldsymbol{P}$ and $\boldsymbol{I}$ from Table 2 are calculated following equations 10–11 and then rescaled to sum to 1 (Table 2).

2.2.3 Anthropogenic changes in background climate means

We estimate anthropogenic trends in background mean climate as CMIP6 24-model weighted mean low-pass filtered trends relative to the mean conditions of the pre-anthropogenic baseline of 1851–1900. While the climate of the late 1800s was not entirely free of anthropogenic influence, we treat is as such because the vast majority of anthropogenic forcing has occurred since that time. This approach is in line with prior efforts to approximate anthropogenic climate trends as those that have occurred since 1901 (Abatzoglou and Williams, 2016; Williams et al., 2015, 2020). To reduce the effect of internal climate variability on modeled trends, we consider as many realizations of Historical and SSP2-4.5 simulated climate as possible for each model. First, for each model we temporally append all pairs of Historical (1850–2014) and SSP2-4.5 (2015–2100) realizations with common variant IDs (e.g., r1i1p1f1), as these realiza-

Table 2. CMIP6 model global mean temperature change (dTave) based on least-squares linear regression from 1961–2025, bias compared to observations, performance weightings based on agreement with the observed temperature trend, independence weightings, and the final weightings (w; Eq. 9) used to estimate anthropogenic climate trends (Sect. 2.2.2). For each model, dTave is the average of linear temperature changes calculated from all available (N) continuous ensemble members covering the Historical and SSP2-4.5 scenarios. Bias is dTave minus the observed global mean temperature trend of +1.183 °C. The observed trend considered here is the average of trends from three observational datasets (NOAA: +1.142 °C; NASA GISS: +1.184 °C; Berkeley Earth: +1.223 °C). Performance values are values of $\boldsymbol{P}$ calculated from Eq. (10), representing how closely each model's simulated temperature trend agrees with observations. Independence values are values of $\boldsymbol{I}$ calculated from Eq. (11), representing how dissimilar each model's ensemble-mean maps of climatological mean surface air temperature and sea-level pressure are to those of all other models.

	dTave (°C)	Bias (°C)	Performance ($\boldsymbol{P}$)	Independence ($\boldsymbol{I}$)	Weighting ($\boldsymbol{w}$)	N
ACCESS-CM2	+1.439	+0.256	0.0052	0.8913	0.0011	3
ACCESS-ESM1-5	+1.377	+0.194	0.0304	1.0000	0.0070	19
CESM2	+1.361	+0.179	0.0742	0.6229	0.0106	6
CESM2-WACCM	+1.571	+0.388	6.455×10^{-6}	0.6220	9.212×10^{-7}	3
CMCC-CM2-SR5	+1.294	+0.111	0.3463	0.9961	0.0791	1
CNRM-CM6-1	+1.229	+0.047	0.3789	0.7655	0.0666	10
CNRM-ESM2-1	+1.086	−0.097	0.0713	0.7655	0.0125	9
CanESM5	+2.123	+0.940	5.188×10^{-31}	1.0000	1.191×10^{-31}	50
EC-Earth3	+1.344	+0.161	0.0071	0.5186	0.0008	21
EC-Earth3-Veg	+1.519	+0.336	8.581×10^{-6}	0.5186	1.021×10^{-6}	8
FGOALS-g3	+1.215	+0.032	0.7696	1.0000	0.1766	4
GFDL-ESM4	+1.222	+0.039	0.1055	1.0000	0.0242	3
HadGEM3-GC31-LL	+1.950	+0.767	6.969×10^{-21}	0.6680	1.068×10^{-21}	1
INM-CM4-8	+1.018	−0.165	0.1076	0.9463	0.0234	1
INM-CM5-0	+0.999	−0.183	0.0652	0.9463	0.0142	1
KACE-1-0-G	+1.787	+0.604	3.103×10^{-13}	0.9452	6.729×10^{-14}	3
MIROC-ES2L	+1.103	−0.080	0.5422	1.0000	0.1244	30
MIROC6	+0.955	−0.228	0.0155	1.0000	0.0036	50
MPI-ESM1-2-HR	+1.135	−0.048	0.5378	0.9960	0.1229	2
MPI-ESM1-2-LR	+1.098	−0.084	0.4492	0.9960	0.1027	30
MRI-ESM2-0	+1.355	+0.172	0.0886	1.0000	0.0203	5
NorESM2-LM	+1.124	−0.059	0.6205	0.9947	0.1416	3
NorESM2-MM	+1.065	−0.118	0.3077	0.9702	0.0685	2
UKESM1-0-LL	+1.751	+0.568	8.600×10^{-12}	0.7055	1.392×10^{-12}	14

tions represent continuous runs (ensemble members). However, it is common for more ensemble members to be available for the Historical scenario than for SSP2-4.5. For any model with fewer than 10 continuous ensemble members across the two scenarios, we produce additional sequences of climate by appending combinations of Historical and SSP2-4.5 ensemble members with non-matching variant IDs. This is done either until there are 10 continuous climate records covering 1850–2100 or until all possible pairs of Historical and SSP2-4.5 variant IDs have been combined. The purpose of combining ensemble members is to better capitalize on the available Historical realizations, as most of the 1951–2025 period of our dataset is within the CMIP6 Historical period. Table 1 shows for each model and variable the number of Historical and SSP2-4.5 realizations with monthly data that are used as well as the number of combinations used.

For each climate variable (prec, t_{max}, t_{min}, ea, wind, solar, longwave, psfc), each CMIP6 model, and each combination of Historical and SSP2-4.5 realizations available for that variable-model, we convert the simulation outputs of monthly means to anomalies relative to 1851–1900 for each of the 12 months separately. For all variables except t_{max} and t_{min} we calculate relative anomalies by dividing by the 1851–1900 mean.

Throughout this work, we assess modeled change in non-temperature variables as proportional change (dividing by baseline mean) because proportional changes are less likely to be sensitive to systematic model biases in baseline mean climate. For example, modeled changes in precipitation total in original units of mm d^{-1} tend to scale with background mean precipitation total (wetter places have greater capacity for change). Inter-model differences in background mean precipitation, which can be particularly large in areas of complex topography due to model differences in geographic resolution, will thus contribute directly to model differences in the magnitudes of precipitation change in mm d^{-1} even if all models project the same proportional change. Further, when removing anthropogenic trends from observa-

tions, scaling observations as a proportion of background mean never causes unrealistic negative values. For temperature, there is not a positive relationship between mean background temperature and simulated trends or daily variances, nor is there an issue with unrealistic negative values.

For each of the 12 months, we calculate low-pass filtered time series of trends in these anomalies for each 1° grid cell using a 10-point butterworth filter. For all variables except prec, we use a 75-year filter. For prec we use a 100-year filter to reduce the effect of relatively high decadal variability in that variable. To limit artificial end effects, we pad the beginnings and ends of all times series prior to filtering. At the beginning, we pad each time series with values from 1851 through $1851+N$ in reverse order, where N is the rounded value of the filter window length divided by two. We do the same at the end, using the values from $2100-N$ through 2099, except to avoid reversing anthropogenic trends we detrend these values and superimpose on an extrapolation of the linear trend established during $2100-N$ through 2099.

For each model, variable, and grid-month we then calculate the mean of low-pass filtered anomaly trends across all combinations of Historical and SSP2-4.5 realizations. Finally, the anthropogenic effect on background mean climate anomalies is calculated as the weighted multi-model mean trend.

As an example, Fig. 2a–e shows time series of the western US spatially averaged low-pass filtered trends in annually and seasonally averaged t_{max} anomalies from 1851–2025 relative to the 1851–1900 mean for each of the 24 models as well as the 24-model mean. All models agree on a warming of background mean t_{max} by 2025, with most models agreeing on an increase of 1–2 °C. Note that while Fig. 2a–e (and left-column panels of Figs. 3–4 and A2–A7) shows regionally averaged CMIP6 trends at the annul and seasonal scales for feasibility of display, the trends were quantified at the monthly temporal and 1° spatial scales (and then interpolated to $1/24°$ resolution). Maps in Fig. 2f–j show the spatial distribution of the anthropogenic warming signal on t_{max} as of 2025, indicating generally more warming in the continental interior than near the Pacific coast. Figure A2 shows a version of the same figure for t_{min}, indicating somewhat stronger anthropogenic warming than for t_{max}.

Figure 3a–j is structured the same as in Fig. 2 but for relative changes in background mean prec, showing considerable model disagreement with the exception of increases of 5 %–10 % in winter (December–February) across the central and high latitudes of the western US. Outside of winter (Fig. 3b,g), the anthropogenic forcing on background mean prec is estimated to be relatively flat, though in spring this is because increases of 5 %–10 % in the northern latitudes are compensated by decreases in the southern latitudes (Fig. 3c, h). Figure 4a–j shows relative changes in the background means of annually averaged ea, wind, solar, longwave, and psfc (see panels a–h of Figs. A3–A7 for breakdowns of background mean changes in these variables by season). As of 2025, the CMIP6 weighted-mean trends indicate increases in annually averaged western US ea of approximately 10 %, little change in wind, decreased solar of 1 %–2 %, increased longwave of approximately 4 %, and a clear but negligible increase in psfc of approximately 0.075 %.

2.2.4 Calculating anthropogenic changes in daily variances

We define the anthropogenic effect on daily variances as the weighted, 24-model mean changes in the distributions of daily departures from the trends in background mean states quantified above. Because this step requires more data intensive work with daily CMIP6 data, we use only one continuous Historical-SSP2-4.5 realization per model rather than as many as possible. For each model, we obtain the first realization (e.g., r1i1p1f1) for which daily outputs are available for all necessary climate variables (acknowledging that solar, longwave, and wind outputs were available for 22 of the 24 models we consider, as described in Sect. 2.2.1).

For each model and variable, we convert daily values to departures from the background mean state by dividing by (or subtracting away for temperature variables) the values in that model's all-realization mean low-pass filtered monthly time series. We then quantify changes in the variations between the recent observational period and the second half of the 1800s by quantifying changes in the cumulative distribution functions (CDFs) of daily anomalies. Because anthropogenic forcing should cause daily climate variability to change over time, and because a large number of samples are needed to accurately characterize a distribution, we characterize distributions throughout the 1951–2025 observed period using 15-year CDFs staggered by five years. Specifically, for each of the 12 months and for each model, variable, and 1° grid cell, we use a kernel smoothing function (ksdensity in Matlab R2025b) to calculate the CDF of all daily departures from the low-pass filtered mean climate for each of the 11 following 15-year periods: 1951–1965, 1956–1970, 1961–1975, 1966–1980, 1971–1985, 1976–1990, 1981–1995, 1986–2000, 1991–2005, 2006–2020, and 2011–2025. For each CDF calculated, we estimate the 101 data values that correspond to 101 evenly spaced quantiles from zero to one.

We then assess each model's anthropogenically forced change in daily distributions as the difference in the CDF for a given 15-year observational period of interest (e.g., 1956–1970) and the mean CDF from four distinct 15-year periods that begin in the 19th-century portion of the CMIP6 Historical scenario (1851–1865, 1866–1880, 1881–1895, 1896–1910). We characterize the pre-anthropogenic distribution as the mean of multiple 15-year CDFs rather than as a single CDF for consistency with the 15-year period used for the observed-period CDFs. Finally, for each of the 11 observational 15-year periods, we calculate the anthropogenic effect on daily variability as the CMIP6 weighted 24-model

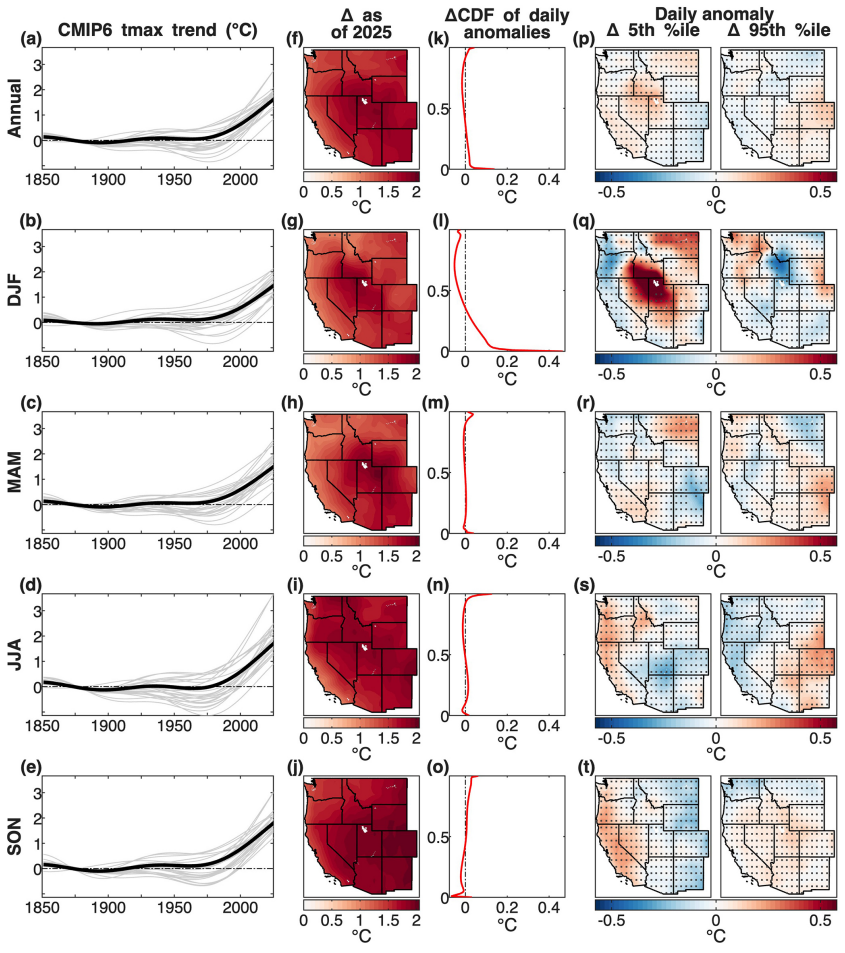

Figure 2. Anthropogenic trends in background means and daily distributions of daily maximum temperature (t_{max}). Time series panels on left **(a–e)** show trends in mean annual (January–December) and seasonal (DJF: December–February, MAM: March–May, JJA: June–August, SON: September–November) western US t_{max} according to (grey thin lines) each of 24 CMIP6 models and (black bold line) the multi-model mean from 1851–2025. Trends expressed as deviations from the 1851–1900 mean. Maps in **(f)–(j)** show multi-model mean trend magnitudes as of 2025. Red curves in **(k)–(o)** show the multi-model mean change in the cumulative distribution function (CDF) of daily anomalies (departures from the background mean trends) between 2011–2025 and 1851–1910 (black dotted line shows zero change). For a given quantile value (y axis), the x axis value is the anomaly expected during 2011–2025 minus that expected in 1851–1910. Pairs of maps on the right **(p–t)** show multi-model mean (left) 5th and (right) 95th percentiles of daily anomalies during 2011–2025 minus those of 1851–1910. Daily anomalies are calculated relative to trends in background means. In maps, stippling indicates that fewer than two-thirds of models agree on the sign. Multi-model means are calculated using the weighted means shown in Table 2, as described in Sect. 2.2.1.

mean difference between the observed-period CDF and the pre-anthropogenic CDF. For each non-temperature variable, the change in CDFs is assessed as, for each of the 101 evenly spaced quantiles, the corresponding daily anomaly value in the observed period's CDF divided by that of the pre-anthropogenic CDF. For temperature, the change is quantified by subtracting the pre-anthropogenic CDF values from the observed-period CDF values.

Figure 2k–o shows how the western US CMIP6 weighted-mean CDF of daily t_{max} anomalies relative to the background mean trend during 2011–2025 compares to that of the pre-anthropogenic period on annual and seasonal scales. The corresponding maps in Fig. 2p–t show how changes the 5th and 95th percentile t_{max} anomalies are distributed spatially. Overall models disagree regarding changes in the distribution of daily t_{max} anomalies with the exception of warming of the coolest t_{max} anomalies in winter of over 0.5 °C across the northern portion of the Great Basin (Fig. 2l, q). Simulated changes in distributions of daily t_{min} anomalies are similar to those of t_{max} with the exception of a stronger tendency toward reduced winter extremes (warmer lows and cooler highs) east of the Cascades Range in the northwestern US as well the Great Basin (Fig. A2k–p).

Figure 3k–o shows CMIP6 weighted-mean changes in the CDFs of daily non-zero (≥ 0.1 mm) prec anomalies, again comparing distributions during 2011–2025 to those of the

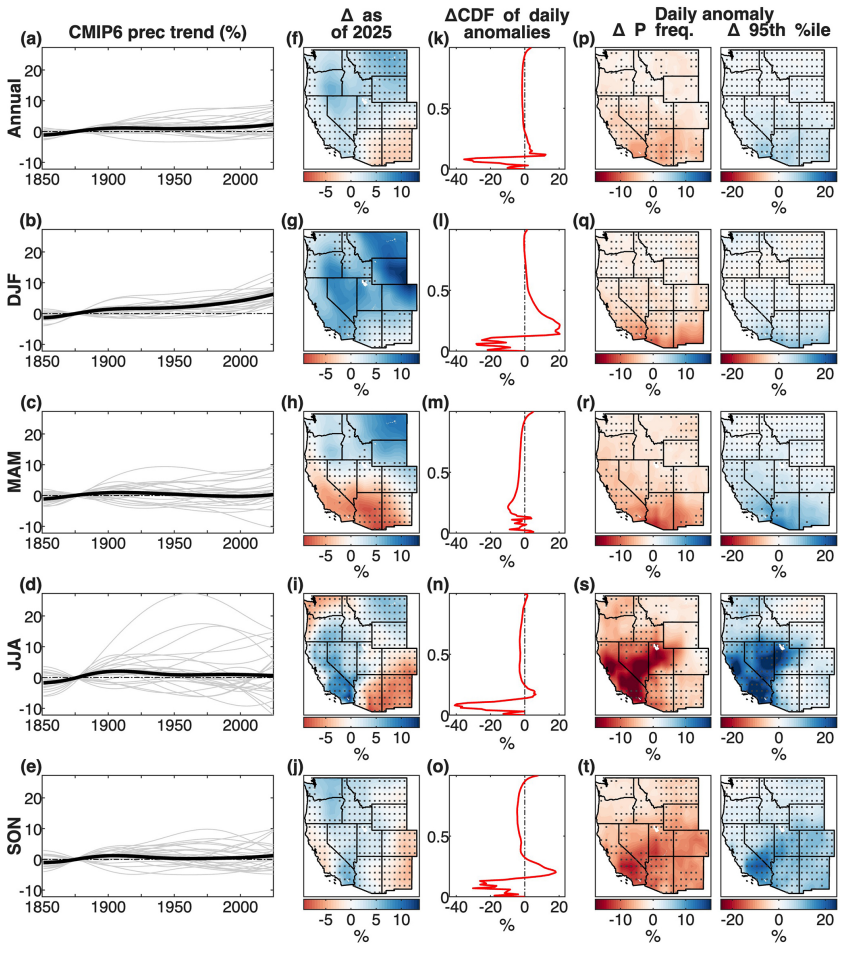

Figure 3. Anthropogenic trends in background means and daily distributions of precipitation total (prec). Time series panels on left **(a–e)** show trends in mean annual (January–December) and seasonal (DJF: December–February, MAM: March–May, JJA: June–August, SON: September–November) western US prec according to (grey thin lines) each of 24 CMIP6 models and (black bold line) the multi-model mean from 1851–2025. Trends expressed as percent deviations relative to the 1851–1900 mean. Maps in **(f)–(j)** show multi-model mean trend magnitudes as of 2025. Red curves in **(k)–(o)** show the multi-model mean change in the cumulative distribution function (CDF) of daily non-zero prec anomalies (departures from the background mean trends) between 2011–2025 and 1851–1910 (black dotted line shows zero change). For a given quantile value (y axis), the x axis value is the non-zero prec anomaly expected during 2011–2025 relative to that of 1851–1910. Pairs of maps on the right **(p–t)** show multi-model mean (left) percent change in the frequency of non-zero prec days (P freq) and (right) 95th percentile anomalies of daily non-zero prec during 2011–2025 relative to those of 1851–1910. Daily anomalies are calculated relative to trends in background mean trends. In maps, stippling indicates that fewer than two-thirds of models agree on the sign of the value. Multi-model means are calculated using the weighted means shown in Table 2, as described in Sect. 2.2.1.

pre-anthropogenic period. In all seasons, models simulate reduced prec anomalies among the driest 10 %–20 % of days with non-zero prec totals. The pairs of maps in Fig. 3p–t show changes in the frequency of days with non-zero prec as well as changes in the 95th percentile of non-zero prec anomalies relative to the background mean. The weighted-model mean indicates reduced prec frequency, particularly in spring–fall, of 5 %–10 % and increases in the most extreme precipitation anomalies (e.g., 95th percentile). Note that because daily prec anomalies are assessed as proportional to (percent of) the background mean, an increase in the background mean of, say, 10 % automatically implies the expectation of a corresponding 10 % increase in non-zero daily prec totals. Thus, any changes in daily non-zero prec anomalies shown in Fig. 3k–t represent changes after accounting for the proportional trends in background mean totals shown in Fig. 3a–j. This explains why models disagree regarding change in the 95th percentile of daily non-zero prec anomalies in winter (Fig. 3q) despite strong agreement on increases in background mean winter prec totals (Fig. 3b, g). Likewise, although CMIP6 models generally simulate historical increases in winter–spring 95th percentile prec totals in winter–spring in the northern latitudes of the western US (Williams et al., 2024a), this is largely accounted for by the simulated

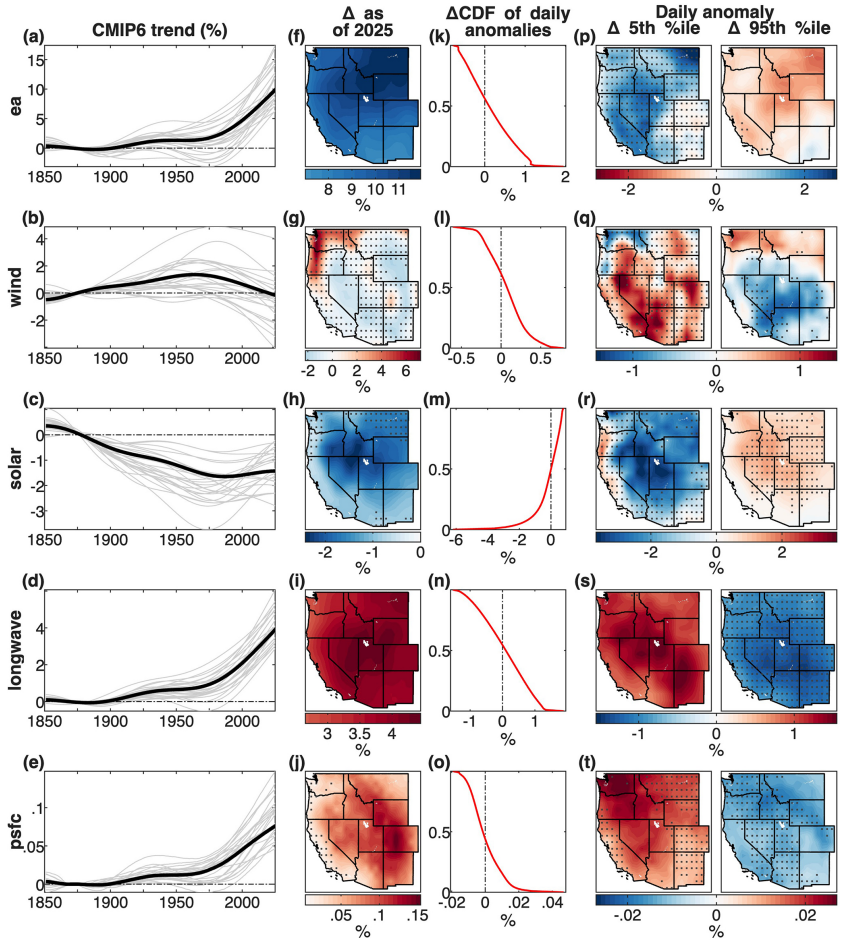

Figure 4. Anthropogenic trends in background means and daily distributions of vapor pressure (ea), wind speed (wind), downward solar and longwave radiation at the surface (solar and longwave, respectively), and surface pressure (psfc). Time series panels on left **(a–e)** show trends in mean annual anomalies for each variable averaged across the western US according to (grey thin lines) each of 24 CMIP6 models and (black bold line) the multi-model mean from 1851–2025. Trends expressed as percent deviations relative to the 1851–1900 mean. Maps in **(f)–(j)** show the multi-model mean trend magnitude as of 2025. Red curves in **(k)–(o)** show the multi-model mean change in the cumulative distribution function (CDF) of daily anomalies (departures from the background mean trends) between 2011–2025 and 1851–1910 (black dotted line shows zero change). For a given quantile value (y axis), the x axis value is the daily anomaly value expected during 2011–2025 relative to that expected in 1851–1910. Pairs of maps on the right **(p–t)** show multi-model mean (left) 5th and (right) 95th percentile anomalies of daily climate during 2011–2025 minus those of 1851–1910. In all analyses of daily anomalies, anomalies are calculated relative to trends in background mean trends. In maps, stippling indicates that fewer than two-thirds of models agree on the sign. Multi-model means are calculated using the weighted means shown in Table 2, as described in Sect. 2.2.1.

increase in background mean prec and the only places where 95th percentile anomalies relative to background means increase in the cool season are where the background mean trend is negative (Fig. 3l, m, q, r). On the other hand, CMIP6 models simulate enhanced daily summertime prec anomalies to become 10 %–20 % more intense relative to the background mean across California and the Great Basin region (Fig. 3n) despite moderate increases of approximately 5 % in background mean totals (Fig. 3i).

Figure 4k–t shows the CMIP6 weighted-mean changes daily anomaly distributions at the annual scale for ea, wind, solar, longwave, and psfc. See Figs. A3–A7 for changes in distribution by season for these variables. For ea, models suggest contracted distributions of daily anomalies, with stronger agreement on weakened positive anomalies than negative anomalies (Fig. 4k, p). Models also suggest contracted distributions of wind anomalies across much of the western US (Fig. 4l, q). There is relatively strong inter-model agreement on widening of the distribution of daily solar anomalies (Fig. 4m, r), driven mostly by decreases in the most negative winter and spring anomalies of 5 %–10 % relative to the background mean, which is also reduced by approximately 1 %–3 % in these seasons relative to the pre-anthropogenic mean (Fig. A5). Models show strong agree-

ment on a contracted distribution of daily longwave anomalies across the western US that is year-round, yet relatively small, with the most negative and positive daily departures from the background mean contracting by approximately 1 %–1.5 % (Fig. 4l, p). Contractions of longwave anomalies are largest, closer to 2 %, in winter (Fig. A6). Models also generally suggest contracted distributions of daily psfc anomalies, but similar to the simulated increases in background mean psfc, the contraction of daily anomalies is very small (Figs. 4o, t and A7).

2.2.5 Removing anthropogenic effects from observed daily climate

To remove the estimated anthropogenic changes in background means and daily variances described in Sect. 2.2.2 and 2.2.3 from the observed daily dataset described in Sect. 2.1, we remove the anthropogenic trends in background means and then adjust daily variances.

The first step bilinearly interpolates monthly 1° grids of CMIP6 24-model weighted mean anthropogenic trends for the period of 1951–2025 to the 1/24° resolution of the observational dataset. For non-temperature variables, the anthropogenic trend is represented as fractional change relative to the climatological mean of 1851–1900 for each of the 12 months. We thus remove these trends by, for each month from 1951–2025, dividing each day's observed climate map by the corresponding 1/24° map of interpolated fractional change values. The same is done for t_{max} and t_{min} except that anthropogenic trends, which are assessed as °C change from the 1851–1900 mean, are subtracted from observations.

Next, for each of the 12 months and each variable, we use the detrended observations described in the paragraph above to produce an observed CDF of daily anomalies for each 1/24° grid cell for each of the 15-year periods from 1951–2025. For each 15-year period, the anomalies are calculated relative to the mean of that period and are thus meant to represent daily departures from the expected pre-anthropogenic 1851–1900 baseline. The departures are calculated as fraction of the mean for non-temperature variables. We then calculate, for each of the 12 months, each variable, and each 1/24° grid cell, a CDF of these departure values for each 15-year period following the same method applied to the CMIP6 data such that there is an estimated climate value associated with each of 101 quantiles from zero to one.

The next objective is to adjust the distributions of the observed departures from the pre-anthropogenic baseline climatology. This is done by, for each of the 12 months, each variable, each 15-year period from 1951–2025, and each 1/24° grid cell, estimating the pre-anthropogenic CDF and then using quantile mapping to adjust the daily values for that period's central five years accordingly. Recall from Sect. 2.2.3 that the anthropogenic effect on daily variances in a given 15-year period from the observational era was calculated as the observational-era CDF divided by the pre-anthropogenic CDF for non-temperature variables, and as the observational-era CDF minus the pre-anthropogenic CDF for temperature. (For prec, there is an additional step to adjust for CMIP6 changes in the frequency of days with non-zero prec. Where the adjustment requires a change in prec frequency (pre-anthropogenic frequency was different from that of the modern 15-year period of interest), the adjusted CDF of observed daily prec anomalies is adjusted again to reflect the correct proportion of non-zero prec days while not changing the sum of anomalies on days with non-zero prec.) Thus, for each 15-year period during 1951–2025 and each of 101 quantiles from zero to one, we have a 1°-resolution map of how anthropogenic forcing is estimated to have altered that quantile's associated daily departure values. We bilinearly interpolate these maps to 1/24° resolution, resulting in, for each of the 12 months, each variable, each 15-year period in the observational era, and each 1/24° grid cell, a set of 101 CDF adjustment values that can be used to transform the observed daily climate anomalies to take on a distribution consistent with that expected from the pre-anthropogenic era.

Finally, we use quantile mapping to transform the observed daily departures from the pre-anthropogenic background mean to take on the pre-anthropogenic distribution. For each variable, each of the 12 months, each observed-era 15-year period, and each 1/24° grid cell, we convert the observed daily departures from the pre-anthropogenic background means to quantiles. For the central 5 years of each 15-year period (but the first 10 years of the first 15-year period and last 10 years of the last 15-year period), we then use linear interpolation to associate each quantile value with the expected daily departure value expected of the pre-anthropogenic distribution. We then impose these adjusted daily departures back onto the pre-anthropogenic background mean by, for non-temperature variables, multiplying the adjusted departures by the 15-year period's pre-anthropogenic mean. For temperature, the adjusted departures are added to the 15-year pre-anthropogenic mean. In so doing, we produce full time series of daily data at 1/24° resolution that follow the observed sequence of daily to decadal climate variability from 1951–2025, but without CMIP6 24-model weighted mean trends in background means or daily variability.

While the above procedure automatically reduces the prec frequency where CMIP6 models indicate pre-anthropogenic prec frequency was lower by adjusting some number of the lowest daily non-zero prec totals to zero, it does not automatically adjust observations of zero prec to non-zero values where CMIP6 models indicate pre-anthropogenic prec frequency was higher. To increase prec frequency in a given grid cell (cell i), we estimate that the observed zero prec days most likely to have non-zero prec under pre-anthropogenic forcings are those when prec totals in nearby areas are highest. Specifically, if n days with zero prec need to have non-zero prec for cell i in a given 15-year period, we identify the n days during that period with the highest prec averaged

across all cells within a 0.25° geographic radius centered on i. If there are fewer than n days with non-zero mean prec within the 0.25° radius, the radius is expanded by 0.25° and so on until n days of non-zero mean prec are identified. If more than n days are identified that meet this criterion, the n days with largest mean prec totals in the surrounding area are selected as days to assign non-zero prec values to cell i. To determine how much prec to assign to cell i on the chosen n days, we produce a CDF of all regionally averaged non-zero prec values for the surrounding area and determine the quantile values associated with the n days of interest. We then use quantile mapping to translate these n quantile values to prec totals for cell i based on the expected pre-anthropogenic CDF of non-zero prec totals for cell i. After correcting for changes in non-zero prec frequency, daily prec totals for each grid cell, each of the 12 months, and each 15-year period are rescaled as needed to assure that they average to equal that of the pre-anthropogenic mean.

3 Data Overview

The datasets provided are monthly netcdf files of observed and CMIP6-detrended daily 1/24° resolution gridded maps of prec, t_{max}, t_{min}, ea, wind, solar, longwave, and psfc across the western US (11 westernmost states of the coterminous US) from 1 January 1951 through 31 December 2025. Figures 5–6 and A7–A10 provide time series and distribution plots that visualize western US regionally averaged trends and ranges of daily variability within the observed and CMIP6-detrended datasets. Specifically, Fig. 5 shows observed and CMIP6-detrended time series of annual and seasonally averaged t_{max} and t_{min} from 1951–2025 as well as annual and seasonal distributions of daily t_{max} and t_{min} values for the 2011–2025 period. Figure 6 shows observed and CMIP6-detrended time series and distributions of prec at the annual and seasonal scales. The left column shows western US regionally averaged prec anomalies, the center column shows distributions of daily non-zero prec anomalies, and the right column shows time series of anomalies in the frequency of days with non-zero prec. Figure A8 shows annual and seasonal time series and daily distributions of western US ea and wind, Fig. A9 shows the same for solar and longwave, and Fig. A10 shows the same for psfc.

The variables represented in the ParallelClim-WestUS-Daily dataset can be used to derive many additional variables. For example, two derived variables often used to assess atmospheric aridity are vapor-pressure deficit (vpd; es – ea) and relative humidity (RH; ea/es · 100). See Fig. A11 for time series and daily distributions of western US regionally averaged vpd and RH. To derive these variables we calculate es as the mean of es_{max} and es_{min}, calculated from Eqs. (2) and (3).

A limitation of ParallelClim-WestUS-Daily is that our approach cannot discern geographic patterning of anthropogenic climate change at a finer spatial resolution than that of the CMIP6 models. This limitation is particularly relevant in topographically complex areas where the impacts of anthropogenic forcing are not likely to be geographically smooth, with elevation-dependent effects being dominated by changes in surface albedo, specific humidity, and atmospheric aerosols (Pepin et al., 2025). For example, anthropogenically forced snowpack loss, and thus surface warming due to reduced albedo, should exhibit fine-scale geographic variations (e.g., distinct elevation and slope/aspect bands) and seasonality that differ from how snow-albedo feedbacks are represented in models (Letcher and Minder, 2015; McCrary et al., 2022). Additionally, anthropogenic forcing is expected to weaken the orographic effects on precipitation, including the orographic enhancement on windward sides and the rain-shadow effect on leeward sides (Siler and Roe, 2014; Koszuta et al., 2024). In approximating the anthropogenic effect on precipitation totals as a geographically smooth map of proportional change, our approach misses important fine-scale effects of climate change driven by sharp gradients in topography. Future statistical downscaling efforts should explore incorporating finer-scale topographic adjustments to anthropogenic trends as inferred from regional dynamically downscaled simulations.

Another limitation is that the true anthropogenic contribution to observed climate is not perfectly represented by the CMIP6 24-model weighted mean that we treat as our best approximation of anthropogenic climate change. In particular, there is a high degree of inter-model spread in terms of historical trends in background mean prec (Fig. 3). In winter, when all models evaluated simulate positive trends and the 24-model mean change in background mean prec as of 2025 (relative to 1851–1900) is +8 %, the inter-model range is +4 % to +14 %. Given that the surface water balance and related variables such as streamflow and plant moisture content would be sensitive to even small changes in background mean prec, assessments of anthropogenic forcing on these variables are highly sensitive to uncertainties (Williams et al., 2020).

Additionally, we only use a single ensemble member per model to estimate anthropogenic effects on daily variances. Ideally we would use as many ensemble members as possible, as we do for background mean trends, but this would increase computational expense considerably. However, anthropogenic changes in daily variances are generally much smaller than changes in background means, and thus background means are likely to account for most of the uncertainty in our assessment of anthropogenic climate change.

Related to this, we assume in our counterfactual-climate approach that a world free of anthropogenic forcing would have experienced the same sequence of climatic variations as was observed in the anthropogenically forced world. In reality, with or without anthropogenic forcing, natural variability alone would dictate that any alternative realization of the past would follow a sequence of climate variations

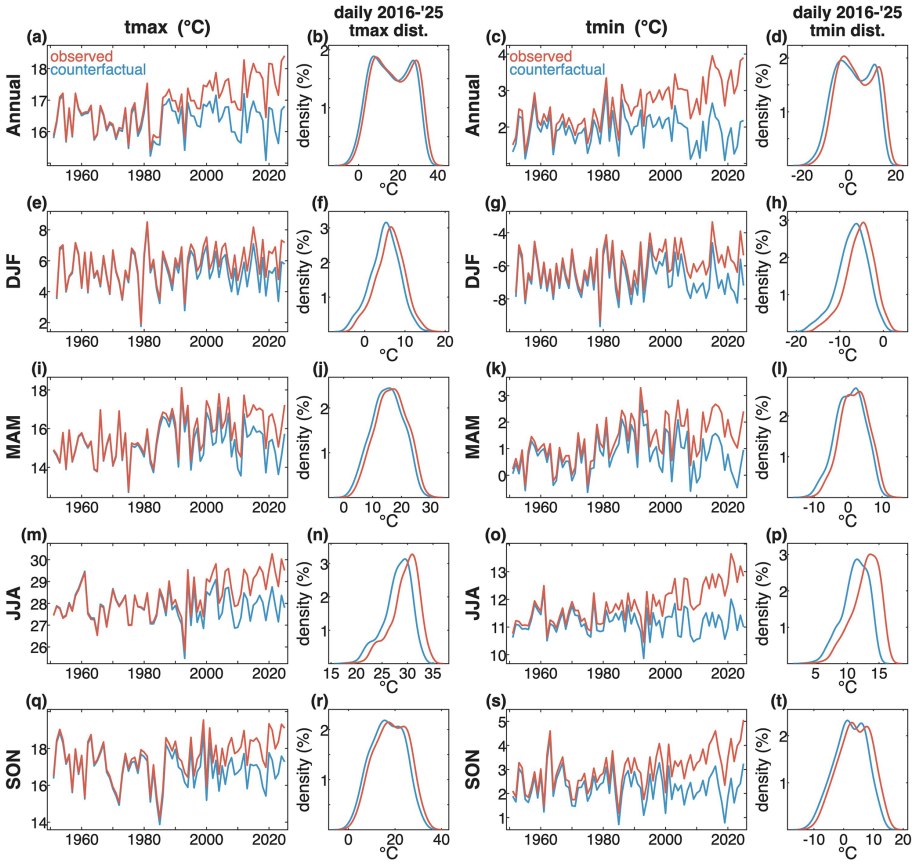

Figure 5. Observed and CMIP6-detrended daily maximum and minimum temperature (t_{max} and t_{min}, respectively) averaged across the western US. **(a, c)** Time series of mean annual t_{max} and t_{min} anomalies, respectively, according to observations (orange) and the CMIP6-detrended dataset (blue). **(b, d)** Kernal density plots of daily t_{max} and t_{min}, respectively, during 2016–2025. The following rows are as in **(a)–(d)** but for seasons (DJF: December–February, MAM: March–May, JJA: June–August, SON: September–November).

largely distinct from those that arose in the observed world. Further, in a counterfactual realization of the absence of anthropogenic forcing, the effects of natural, externally forced variations such as volcanic events and solar cycles may have differed. Thus, the assumption of an observed sequence of variations in the counterfactual world free of anthropogenic forcing is not valid. Nonetheless, this assumption has proven useful for estimates of how anthropogenic forcing may have contributed to an observed climate event or trend of interest (Williams et al., 2015; Abatzoglou and Williams, 2016; Deser et al., 2016; Sippel et al., 2020; Williams et al., 2020, 2024b).

Any use of climate models to estimate the effects of anthropogenic forcing on climate is subject to underlying errors in the climate models themselves. Of particular relevance to western US hydroclimate is uncertainty in anthropogenic effects on ocean circulation and ocean-atmosphere coupling in the tropical Pacific. In particular, the El Niño-Southern Oscillation (ENSO), as well as the Pacific Decadal Oscillation (PDO) of the North Pacific, which is coupled to the ENSO (Newman et al., 2016), are important drivers of natural variability in western US hydroclimate, largely by modulating the latitude of the cool-season jet stream and storm tracks (Ropelewski and Halpert, 1986; Dettinger et al., 1998; Gershunov and Barnett, 1998; Cayan et al., 1999; McCabe and Dettinger, 1999). Over the past approximately four decades, Pacific sea-surface temperatures (SSTs) trended toward the La Niña phase of ENSO and the cool phase of the PDO, both of which are associated with negative precipitation anomalies in the western US (Lehner et al., 2018; Seager et al., 2023; Jiang et al., 2024). While multidecade variations in the ENSO and PDO are expected to be dominated by natural variability, there is much debate about the role for anthropogenic forcing, largely because the recent observed La Niña-like trend is in contrast to the more El Niño-like trends simulated by most climate models (Seager et al., 2019; Cai et al., 2021; Seager et al., 2022; Byrne et al., 2025). While the discrepancy between observed and modeled tropical Pacific trends may be due simply to an improbable natural variation in the observed climate, apparent model biases in ocean-atmosphere coupling over the tropical Pacific may indicate a systematic bias among models (Jiang et al., 2025). In this

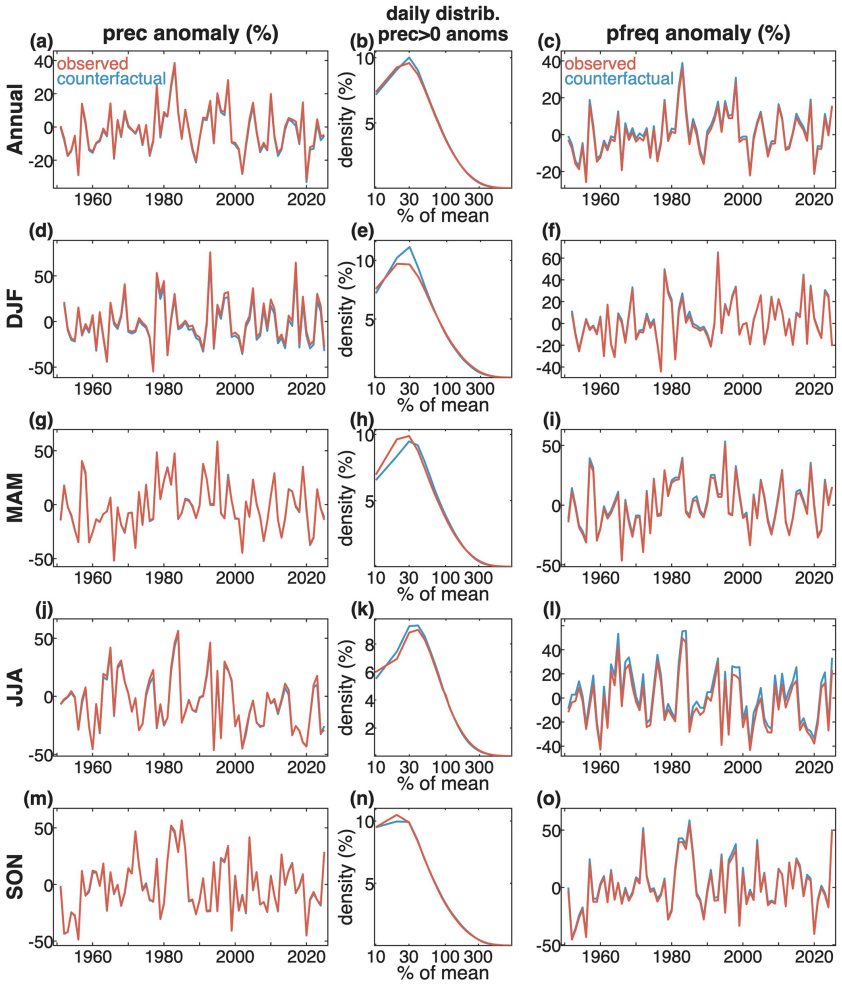

Figure 6. Observed and CMIP6-detrended precipitation (prec) anomalies averaged across the western US. **(a)** Time series of regionally averaged percent anomalies annual precipitation total relative to the 1951–2000 observed mean, according to observations (orange) and the CMIP6-detrended dataset (blue). **(b)** Daily distributions of non-zero precipitation anomalies during 2016–2025 relative to the 1951–2000 observed mean. **(c)** Time series of regionally averaged percent anomalies of annual non-zero precipitation frequency (pfreq). The following rows are as in **(a)**–**(c)** but for seasons (DJF: December–February, MAM: March–May, JJA: June–August, SON: September–November).

case, the true effect of anthropogenic forcing on western US hydroclimate may be not well represented by CMIP6 multi-model mean trends.

Related to the above, our decision to weight the influences of climate models based on their agreement with observed global temperature trends is symptomatic of a suspicion that some CMIP6 models may exhibit sensitivities to anthropogenic forcings that are too strong. Of the 24 models considered, 15 simulate more rapid global warming than was observed from 1961–2025 and half of these simulate a warming that exceeds observations by more than 25 % (0.21 °C) (Table 2). While the slower rate of observed warming relative to that simulated by most models may be due to natural variability, perhaps related to the tropical Pacific trends described above, it may also arise from model biases toward too much sensitivity to greenhouse gas forcing. For example, several models participating in the CMIP6 exhibit a stronger equilibrium climate sensitivity (global surface warming in response to a doubling of atmospheric CO_2 concentration) than did their CMIP5 counterparts (Forster et al., 2020). Further, more CMIP6 models exhibit sensitivities beyond the 4.0 °C upper limit of the "likely" range according to the most recent report by the Intergovernmental Panel on Climate Change (Forster et al., 2020, 2021) and are also beyond the ranges estimated in previous assessments constrained by observations, theory, and paleo-evidence (Knutti et al., 2017b; Zhu et al., 2020). The increase in climate sensitivity among CMIP6 models is due mostly to stronger positive feedbacks with losses of extratropical low clouds and albedo (Zelinka et al., 2020). While much work remains to assess the legitimacy of the modeled low-cloud feedbacks specifically, the shift toward heightened global temperature sensitivity among CMIP6 models is not well supported by observations (Brunner et al., 2020; Liang et al., 2020; Ni-

jsse et al., 2020; Tokarska et al., 2020; Ribes et al., 2021). It is therefore recommended by the authors of the studies cited above and others (Hausfather et al., 2022) to diverge from the historical norm of giving all available models equal weight in assessments of climate sensitivity to a given forcing. Our choice to weight models by their similarity to the recent observed rate of global warming reflects our prioritization of simplicity and interpretability. More complex methods do exist, such as emergent constraints (Hall and Qu, 2006; Cox et al., 2018) and schemes to select or weight models based on skill at simulating multiple climate variables and/or quantities (e.g., means vs trends) for a specific region of interest (Krantz et al., 2022; Pierce et al., 2022). However, applying a more complex model-weighting scheme here would involve subjective decisions regarding which variables and quantities to consider and how they should be prioritized.

4 Data availability

4.1 Datasets used to produce the ParallelClim-WestUS-Daily dataset

We access nClimGrid-daily 1/24° daily prec, t_{max}, and t_{min} (Durre et al., 2022) from https://www.ncei.noaa.gov/products/land-based-station/nclimgrid-daily (last access: 10 November, 2026).

We access PRISM 1/24° daily and 1/120° monthly ea and solar (Daly et al., 2021) from https://prism.oregonstate.edu/ (last access: 10 November 2026).

We access WTK-LED 4 km dynamically downscaled ERA5 hourly 10 m wind (Wang et al., 2024) from https://doi.org/10.25984/2504176.

We access WUS-D3 9 km dynamically downscaled ERA5 daily ea, 10 m wind, solar, and longwave (Rahimi et al., 2024) from https://wrf-cmip6-noversioning.s3.amazonaws.com/index.html#downscaled_products/reanalysis/era5/postprocess/d02/ (last access: 23 November 2025).

We access GridMET 1/24° daily ea, wind, and solar (Abatzoglou, 2013) from https://www.climatologylab.org/gridmet.html (last access: 10 November 2026).

We access NLDAS2 1/8° hourly longwave (Xia et al., 2012) from https://hydro1.gesdisc.eosdis.nasa.gov/data/NLDAS/NLDAS_FORA0125_H.2.0/ (last access: 10 November 2026).

Observed global surface air data come from the National Oceanic and Atmospheric Administration (Huang et al., 2026) (https://www.ncei.noaa.gov/access/monitoring/climate-at-a-glance/global/time-series, last access: 7 April 2026), the National Aeronautics and Space Administration's Goddard Institute for Space Studies (GISTEMP Team, 2024) (https://data.giss.nasa.gov/gistemp/data_v4.html, last access: 7 April 2026), and Berkeley Earth (Rohde and Hausfather, 2020) (https://berkeleyearth.org/data/, last access: 7 April 2026).

CMIP6 climate model simulation outputs were accessed from the Earth System Grid Federation and Oak Ridge National Laboratory (https://esgf-node.ornl.gov/search, last access: 15 April 2026) (Williams et al., 2016).

4.2 ParallelClim-WestUS-Daily

The daily 1/24° observational dataset is available from https://doi.org/10.5281/zenodo.24118479 (Williams, 2026c).

The daily 1/24° counterfactual dataset after removing CMIP6 trends from observations is available from https://doi.org/10.5281/zenodo.20261472 (Williams, 2026b).

5 Code availability

The code to produce the counterfactual dataset as well as the intermediary datasets produced to make the calculations are available from https://doi.org/10.5281/zenodo.20345319 (Williams, 2026a).

6 Summary

ParallelClim-WestUS-Daily is a new pair of parallel datasets of daily, high resolution (∼4 km) gridded surface climate for the western US, representing observed climate from 1951–2025 as well as a counterfactual realization without anthropogenic change in background mean climate or daily variances. Climate variables are precipitation total, maximum and minimum temperature, mean vapor pressure, mean wind speed, mean downward solar and longwave radiation at the surface, and mean surface pressure. Unlike other counterfactual datasets available, ParallelClim-WestUS-Daily uses observational rather than reanalysis sources for precipitation, temperature, and humidity, and other variables are produced by a state-of-the-art dynamically downscaled reanalysis product. This is particularly important for precipitation, as reanalyses commonly misrepresent precipitation extremes and trends (Sun et al., 2018; Hu and Franzke, 2020; Smith et al., 2025). Thus, in addition to the uniquely broad applicability of the counterfactual dataset for evaluation of climate-change impacts in the western US, the observational dataset will, on its own, provide unique value for evaluations of observed hydroclimatic variability, trends, and impacts (Madakumbura et al., 2026), and the 1951–2025 temporal extent will allow for longer temporal context than other observation-based datasets that begin in 1979.

We develop the counterfactual dataset using the "remove-the-modeled-trend" (RTMT) approach, in which anthropogenic trends as simulated by 24 CMIP6 climate models are removed from observations. While it has been standard practice in RTMT approaches to remove anthropogenic trends only from background mean climate, we introduce the advance of also removing trends in daily departures from those background means. This is important because climate

change not only drives changes in background means, but also variability, particularly for precipitation. That said, all counterfactual realizations of observed climate are produced with the simplifying assumption that anthropogenic forcing does not affect atmospheric dynamics. For example, while anthropogenic forcing could conceivably cause a given atmospheric circulation feature to be impossible on a given day, the RTMT method (as well as dynamical downscaling and the regress-out-global-warming method used for the ATTRICI dataset) cannot cancel a circulation event if it occurred in the observed record. These methods can only modify the nature of the event by adjusting precipitation totals, temperature, wind speed, etc. While our removal of anthropogenic effects on daily variability marks an advance, the approach to do so is relatively simple and agnostic to how forced changes to daily variability may vary depending on atmospheric and/or oceanic states. Finally, any model-based calculation of counterfactual climate is subject to climate-model uncertainties and biases. We plan to update the ParallelClim-WestUS-Daily when CMIP7 simulations outputs are available from the next generation of climate models (Dunne et al., 2025).

Finally, a primary motivation behind ParallelClim-WestUS-Daily is to facilitate offline simulations of complex processes downstream of climate and enhance the research community's ability to assess effects of climate change on these processes. Examples of such processes include surface hydrology, vegetation ecosystem dynamics, and wildfire. The ability to monitor climate-change contributions to complex surface processes that are not reliably simulated by global climate models will enable unprecedented guidance as to the rate at which these processes are likely to continue changing in the coming decades.

Appendix A

Table A1. List of the 24 models used and associated references.

Model	Reference
ACCESS-CM2	Bi et al. (2020)
ACCESS-ESM1-5	Ziehn et al. (2020)
CESM2	Danabasoglu et al. (2020)
CESM2-WACCM	Danabasoglu et al. (2020)
CMCC-CM2-SR5	Cherchi et al. (2019)
CNRM-CM6-1	Voldoire et al. (2019)
CNRM-ESM2-1	Séférian et al. (2019)
CanESM5	Swart et al. (2019)
EC-Earth3	Döscher et al. (2022)
EC-Earth3-Veg	Döscher et al. (2022)
FGOALS-g3	Li et al. (2020)
GFDL-ESM4	Dunne et al. (2020)
HadGEM3-GC31-LL	Williams et al. (2018)
INM-CM4-8	Volodin et al. (2017)
INM-CM5-0	Volodin et al. (2018)
KACE-1-0-G	Lee et al. (2020)
MIROC-ES2L	Hajima et al. (2020)
MIROC6	Tatebe et al. (2019)
MPI-ESM1-2-HR	Mauritsen et al. (2019)
MPI-ESM1-2-LR	Mauritsen et al. (2019)
MRI-ESM2-0	Yukimoto et al. (2019)
NorESM2-LM	Seland et al. (2020)
NorESM2-MM	Seland et al. (2020)
UKESM1-0-LL	Sellar et al. (2019)

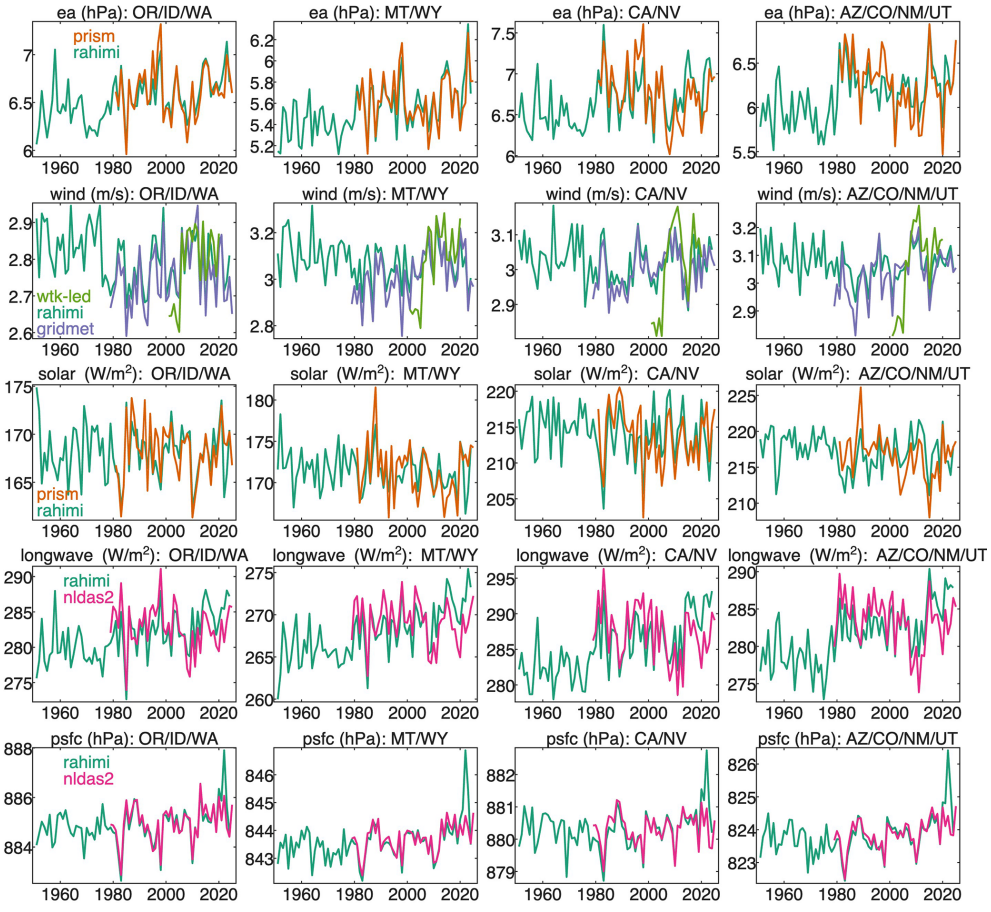

Figure A1. Annual means of the 5 variables for which multiple underlying datasets were used (ea, wind, solar, longwave, and psfc) for each of 4 regions (OR/ID/WA: Oregon, Idaho, Washington; MT/WY: Montana, Wyoming; CA/NV: California, Nevada; AZ/CO/NM/UT: Arizona, Colorado, New Mexico, Utah). In each panel, colors distinguish the dataset shown (legends shown in left-column panels). The first dataset listed in each legend is the dataset treated as the primary dataset, followed by datasets used for years when the primary dataset is not available. For non-primary datasets, the annual means were calculated after the daily data for each 4 km grid cell had been bias corrected with quantile mapping to match daily distributions of the primary dataset.

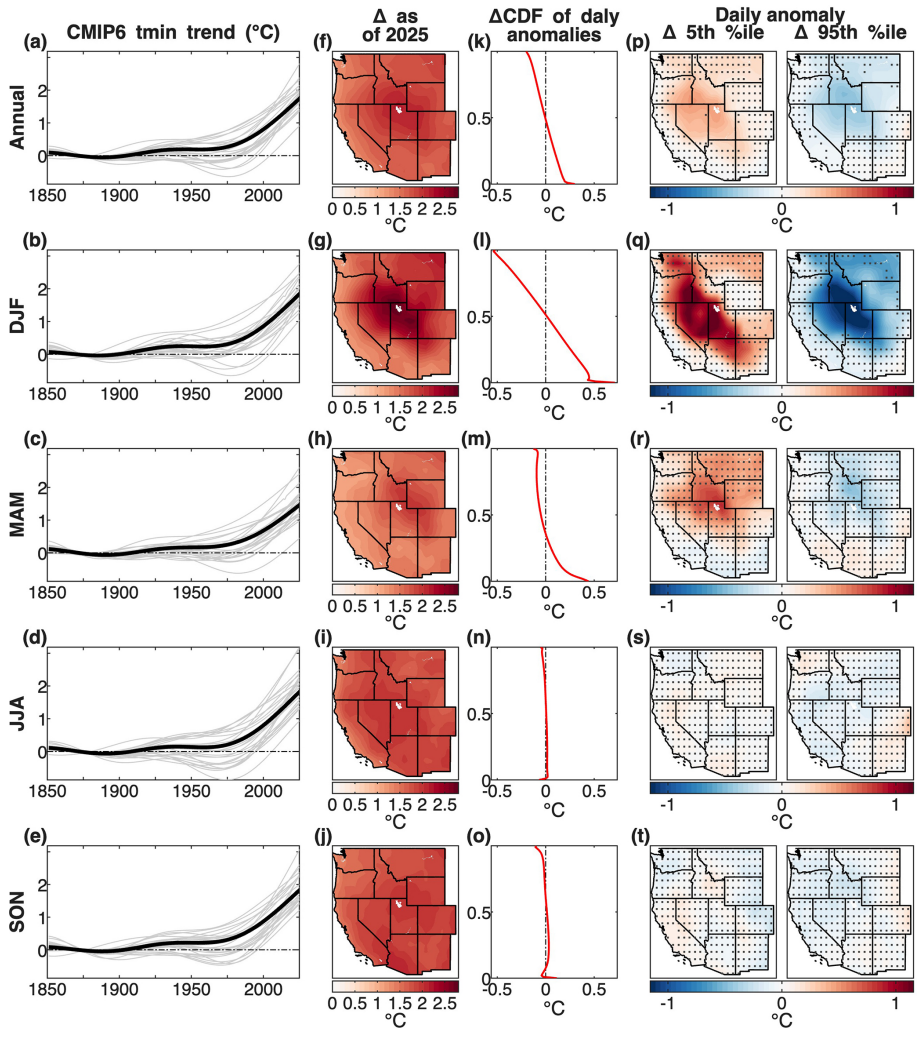

Figure A2. Anthropogenic trends in background means and daily distributions of daily minimum temperature (t_{min}). Time series panels on left **(a–e)** show trends in mean annual (January–December) and seasonal (DJF: December–February, MAM: March–May, JJA: June–August, SON: September–November) western US t_{min} according to (grey thin lines) each of 24 CMIP6 models and (black bold line) the multi-model mean from 1851–2025. Trends expressed as deviations from the 1851–1900 mean. Maps in **(f)–(j)** show multi-model mean trend magnitudes as of 2025. Red curves in **(k)–(o)** show the multi-model mean change in the cumulative distribution function (CDF) of daily anomalies (departures from the background mean trends) between 2011–2025 and 1851–1910 (black dotted line shows zero change). For a given quantile value (y axis), the x axis value is the anomaly expected during 2011–2025 minus that expected in 1851–1910. Pairs of maps on the right **(p–t)** show multi-model mean (left) 5th and (right) 95th percentiles of daily anomalies during 2011–2025 minus those of 1851–1910. Daily anomalies are calculated relative to trends in background means. In maps, stippling indicates that fewer than two-thirds of models agree on the sign. Multi-model means are calculated using the weighted means shown in Table 2, as described in Sect. 2.2.1.

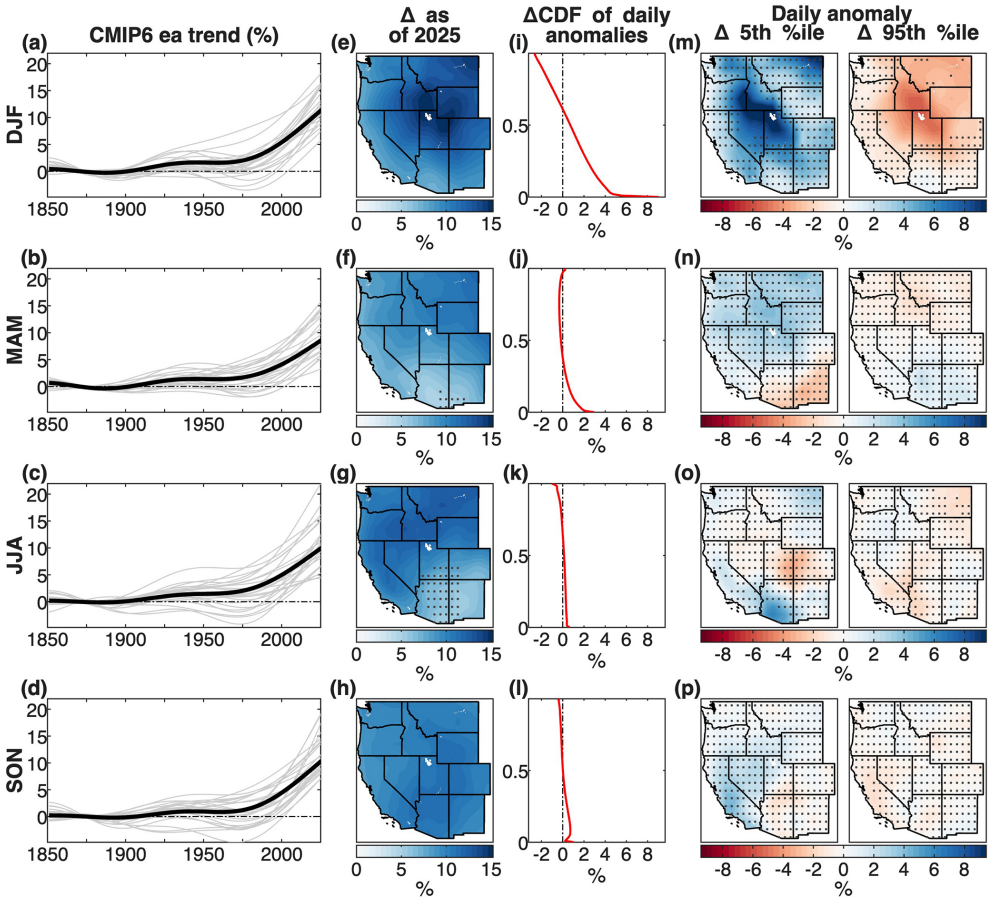

Figure A3. Anthropogenic trends in background means and daily distributions of daily mean vapor pressure (ea). Time series panels on left **(a–d)** show trends in mean seasonal (DJF: December–February, MAM: March–May, JJA: June–August, SON: September–November) western US ea according to (grey thin lines) each of 24 CMIP6 models and (black bold line) the multi-model mean from 1851–2025. Trends expressed as percent deviations from the 1851–1900 mean. Maps in **(e)–(h)** show multi-model mean trend magnitudes as of 2025. Red curves in **(i)–(l)** show the multi-model mean change in the cumulative distribution function (CDF) of daily anomalies (departures from the background mean trends) between 2011–2025 and 1851–1910 (black dotted line shows zero change). For a given quantile value (y axis), the x axis value is the anomaly value expected during 2011–2025 relative to (%) that expected in 1851–1910. Pairs of maps on the right **(m–p)** show multi-model mean (left) 5th and (right) 95th percentiles of daily anomalies during 2011–2025 relative to those of 1851–1910. Daily anomalies are calculated relative to trends in background means. In maps, stippling indicates that fewer than two-thirds of models agree on the sign. Multi-model means are calculated using the weighted means shown in Table 2, as described in Sect. 2.2.1.

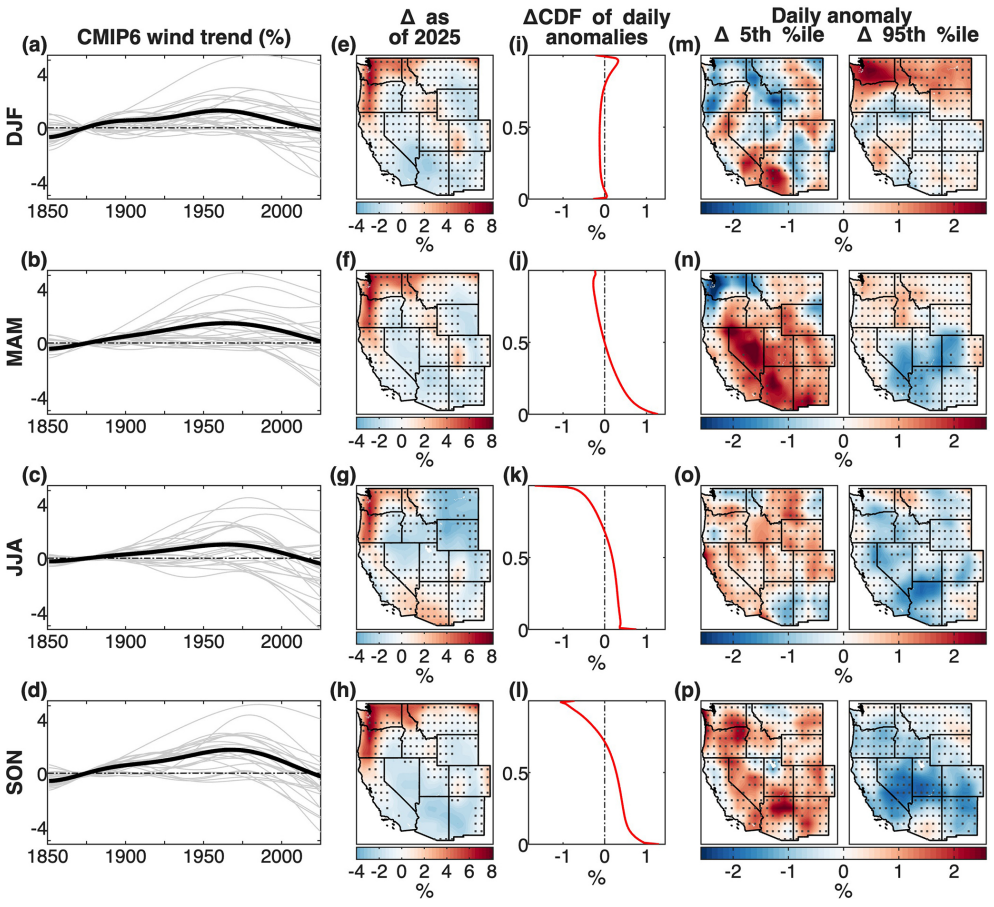

Figure A4. Anthropogenic trends in background means and daily distributions of daily mean 2 m wind speed (wind). Time series panels on left **(a–d)** show trends in mean seasonal (DJF: December–February, MAM: March–May, JJA: June–August, SON: September–November) western US wind according to (grey thin lines) each of 24 CMIP6 models and (black bold line) the multi-model mean from 1851–2025. Trends expressed as percent deviations from the 1851–1900 mean. Maps in **(e)–(h)** show multi-model mean trend magnitudes as of 2025. Red curves in **(i)–(l)** show the multi-model mean change in the cumulative distribution function (CDF) of daily anomalies (departures from the background mean trends) between 2011–2025 and 1851–1910 (black dotted line shows zero change). For a given quantile value (y axis), the x axis value is the anomaly value expected during 2011–2025 relative to (%) that expected in the 1851–1910. Pairs of maps on the right **(m–p)** show multi-model mean (left) 5th and (right) 95th percentiles of daily anomalies during 2011–2025 relative to those of 1851–1910. Daily anomalies are calculated relative to trends in background means. In maps, stippling indicates that fewer than two-thirds of models agree on the sign. Multi-model means are calculated using the weighted means shown in Table 2, as described in Sect. 2.2.1.

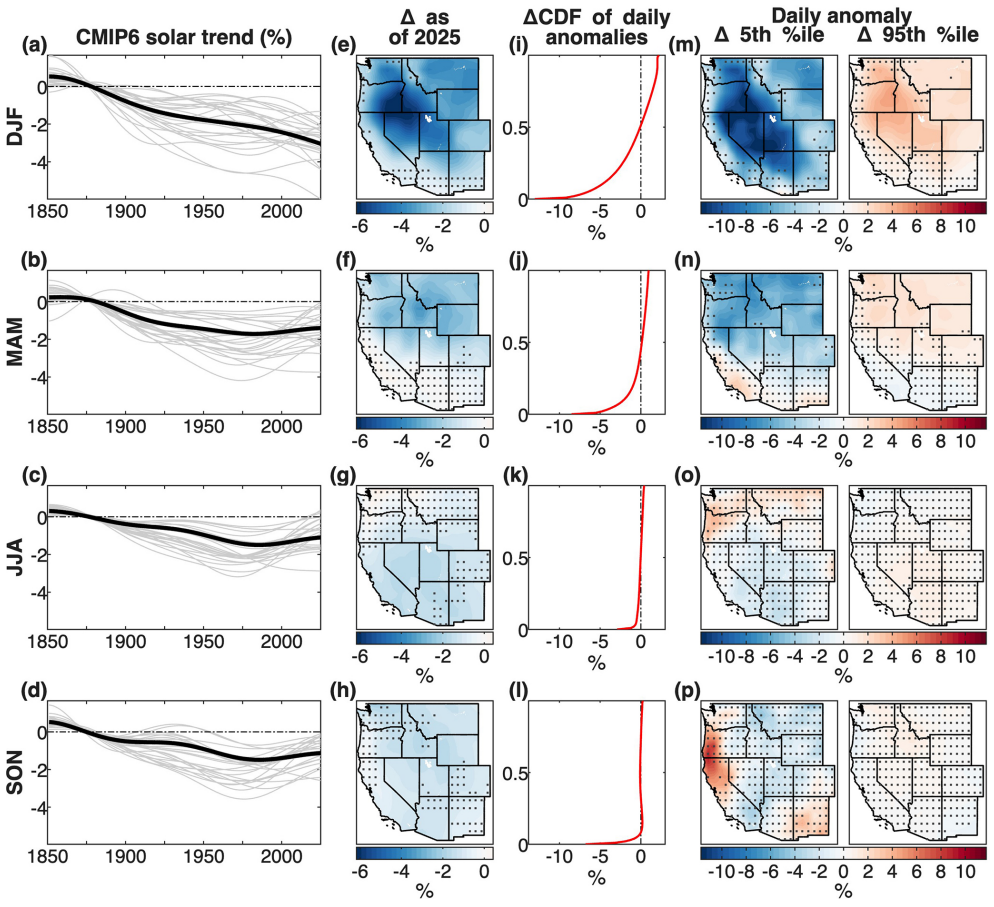

Figure A5. Anthropogenic trends in background means and daily distributions of daily mean downwelling solar radiation at the surface (solar). Time series panels on left **(a–d)** show trends in mean seasonal (DJF: December–February, MAM: March–May, JJA: June–August, SON: September–November) western US solar according to (grey thin lines) each of 24 CMIP6 models and (black bold line) the multi-model mean from 1851–2025. Trends expressed as percent deviations from the 1851–1900 mean. Maps in **(e)–(h)** show multi-model mean trend magnitudes as of 2025. Red curves in **(i)–(l)** show the multi-model mean change in the cumulative distribution function (CDF) of daily anomalies (departures from the background mean trends) between 2011–2025 and 1851–1910 (black dotted line shows zero change). For a given quantile value (y axis), the x axis value is the anomaly value expected during 2011–2025 relative to (%) that expected in 1851–1910. Pairs of maps on the right **(m–p)** show multi-model mean (left) 5th and (right) 95th percentiles of daily anomalies during 2011–2025 relative to those of 1851–1910. Daily anomalies are calculated relative to trends in background means. In maps, stippling indicates that fewer than two-thirds of models agree on the sign. Multi-model means are calculated using the weighted means shown in Table 2, as described in Sect. 2.2.1.

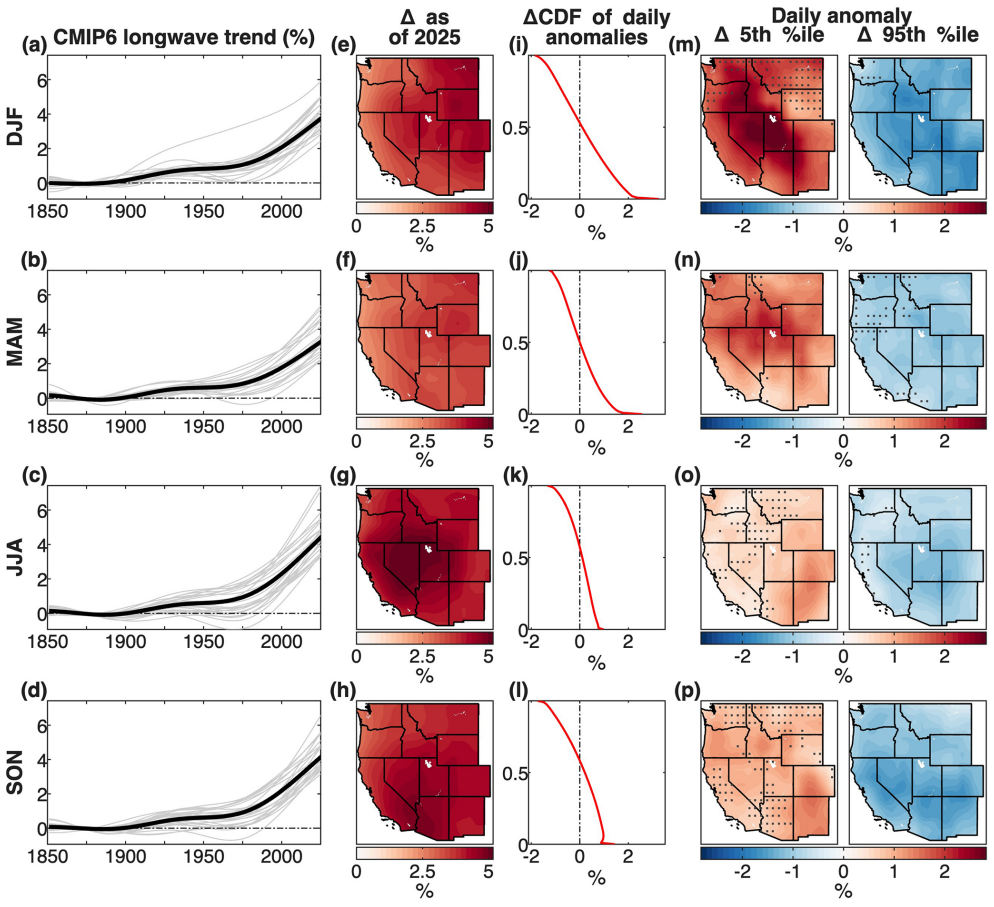

Figure A6. Anthropogenic trends in background means and daily distributions of daily mean downwelling longwave radiation at the surface (longwave). Time series panels on left **(a–d)** show trends in mean seasonal (DJF: December–February, MAM: March–May, JJA: June–August, SON: September–November) western US longwave according to (grey thin lines) each of 24 CMIP6 models and (black bold line) the multi-model mean from 1851–2025. Trends expressed as percent deviations from the 1851–1900 mean. Maps in **(e)–(h)** show multi-model mean trend magnitudes as of 2025. Red curves in **(i)–(l)** show the multi-model mean change in the cumulative distribution function (CDF) of daily anomalies (departures from the background mean trends) between 2011–2025 and 1851–1910. For a given quantile value (y axis), the x axis value is the anomaly value expected during 2011–2025 relative to (%) that expected in the 1851–1910 (black dotted line shows zero change). Pairs of maps on the right **(m–p)** show multi-model mean (left) 5th and (right) 95th percentiles of daily anomalies during 2011–2025 relative to those of 1851–1910. Daily anomalies are calculated relative to trends in background means. In maps, stippling indicates that fewer than two-thirds of models agree on the sign. Multi-model means are calculated using the weighted means shown in Table 2, as described in Sect. 2.2.1.

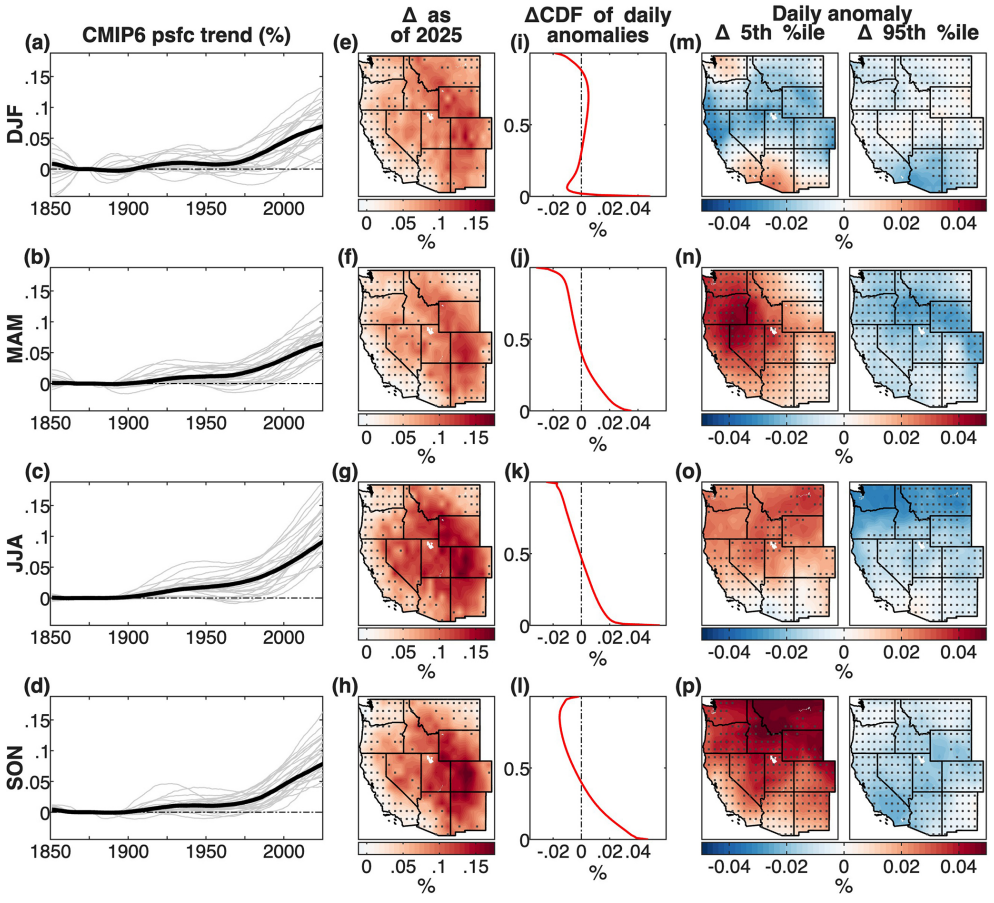

Figure A7. Anthropogenic trends in background means and daily distributions of daily mean surface pressure (psfc). Time series panels on left **(a–d)** show trends in mean seasonal (DJF: December–February, MAM: March–May, JJA: June–August, SON: September–November) western US psfc according to (grey thin lines) each of 24 CMIP6 models and (black bold line) the multi-model mean from 1851–2025. Trends expressed as percent deviations from the 1851–1900 mean. Maps in **(e)–(h)** show multi-model mean trend magnitudes as of 2025. Red curves in **(i)–(l)** show the multi-model mean change in the cumulative distribution function (CDF) of daily anomalies (departures from the background mean trends) between 2011–2025 and 1851–1910 (black dotted line shows zero change). For a given quantile value (y axis), the x axis value is the anomaly value expected during 2011–2025 relative to (%) that expected in the 1851–1910. Pairs of maps on the right **(m–p)** show multi-model mean (left) 5th and (right) 95th percentiles of daily anomalies during 2011–2025 relative to those of 1851–1910. Daily anomalies are calculated relative to trends in background means. In maps, stippling indicates that fewer than two-thirds of models agree on the sign. Multi-model means are calculated using the weighted means shown in Table 2, as described in Sect. 2.2.1.

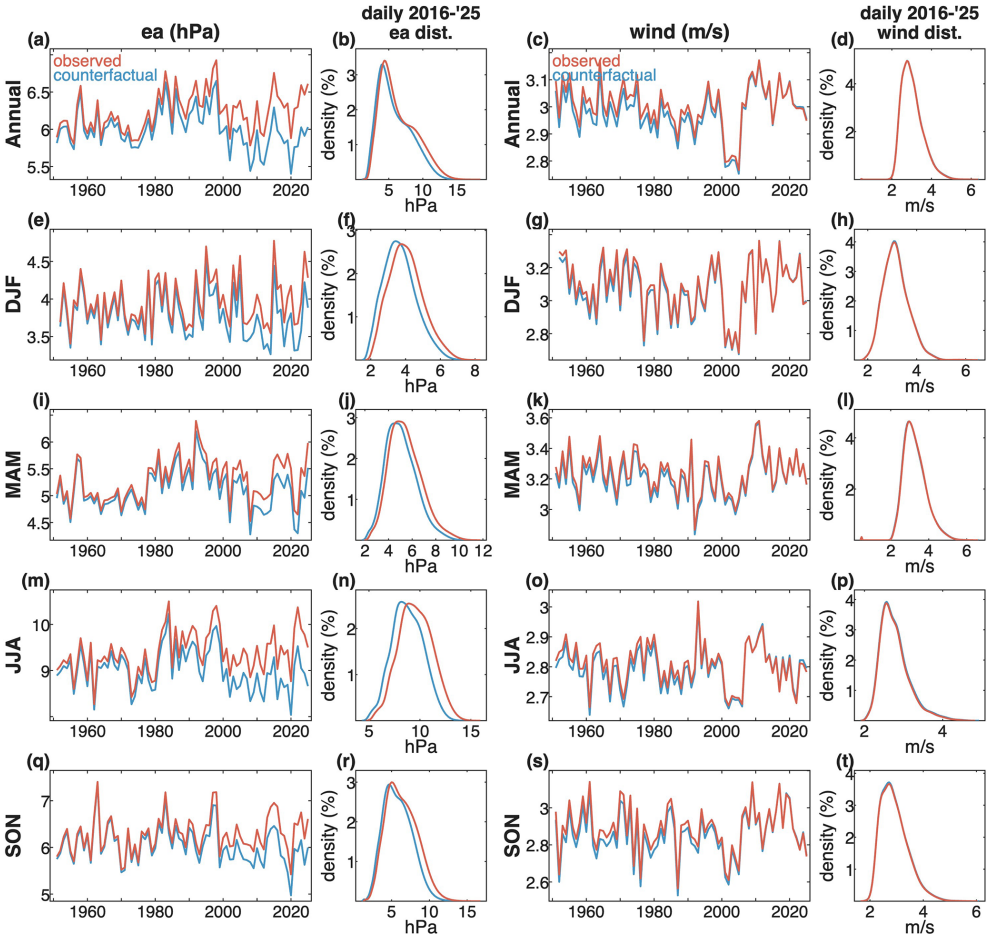

Figure A8. Observed and CMIP6-detrended vapor pressure (ea) and 2 m wind speed (wind) averaged across the western US. **(a, c)** Time series of mean annual ea and wind, respectively, according to observations (orange) and the CMIP6-detrended dataset (blue). **(b, d)** Kernal density plots of daily ea and wind, respectively, during 2016–2025. The following rows are as in **(a)**–**(d)** but for seasons (DJF: December–February, MAM: March–May, JJA: June–August, SON: September–November).

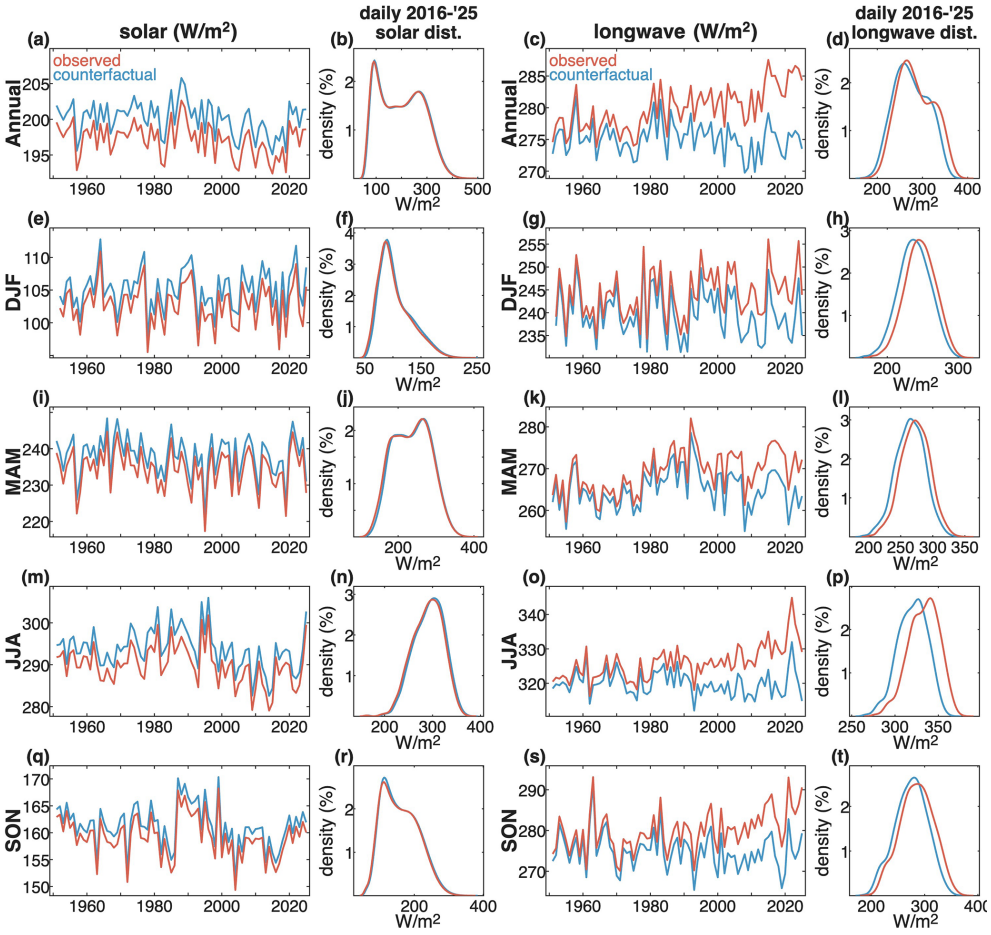

Figure A9. Observed and CMIP6-detrended downwelling solar and longwave radiation at the surface (solar and longwave, respectively) averaged across the western US. **(a, c)** Time series of mean annual solar and longwave, respectively, according to observations (orange) and the CMIP6-detrended dataset (blue). **(b, d)** Kernal density plots of daily solar and longwave, respectively, during 2016–2025. The following rows are as in **(a)**–**(d)** but for seasons (DJF: December–February, MAM: March–May, JJA: June–August, SON: September–November).

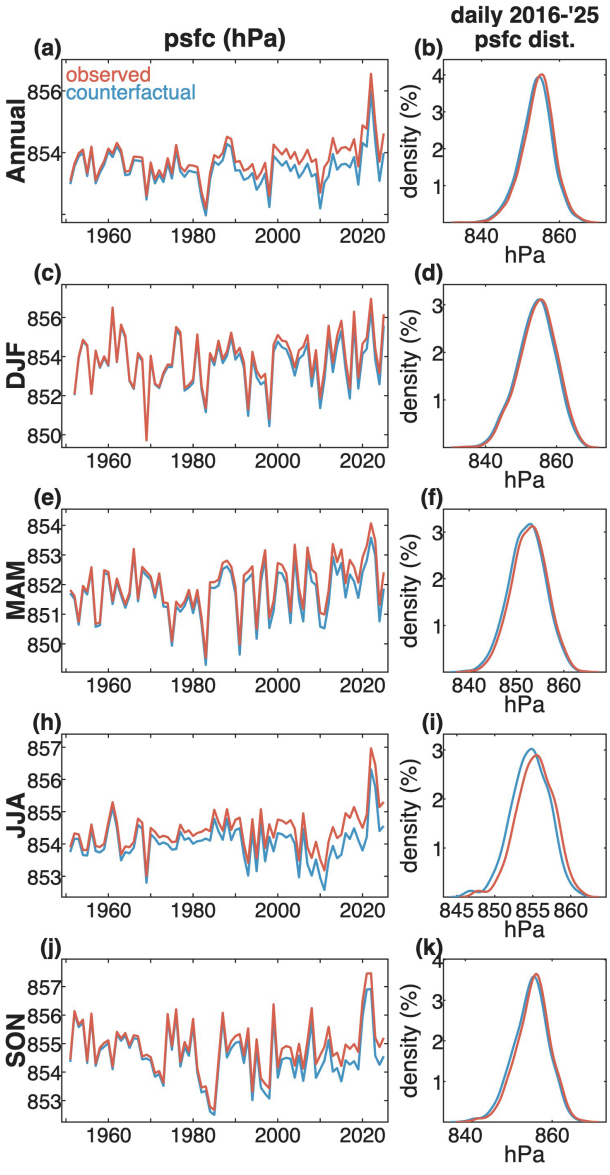

Figure A10. Observed and CMIP6-detrended surface pressure (psfc) averaged across the western US. **(a)** Time series of mean annual psfc according to observations (orange) and the CMIP6-detrended dataset (blue). **(b)** Kernal density plots of daily psfc, during 2016–2025. The following rows are as in **(a)**–**(b)** but for seasons (DJF: December–February, MAM: March–May, JJA: June–August, SON: September–November).

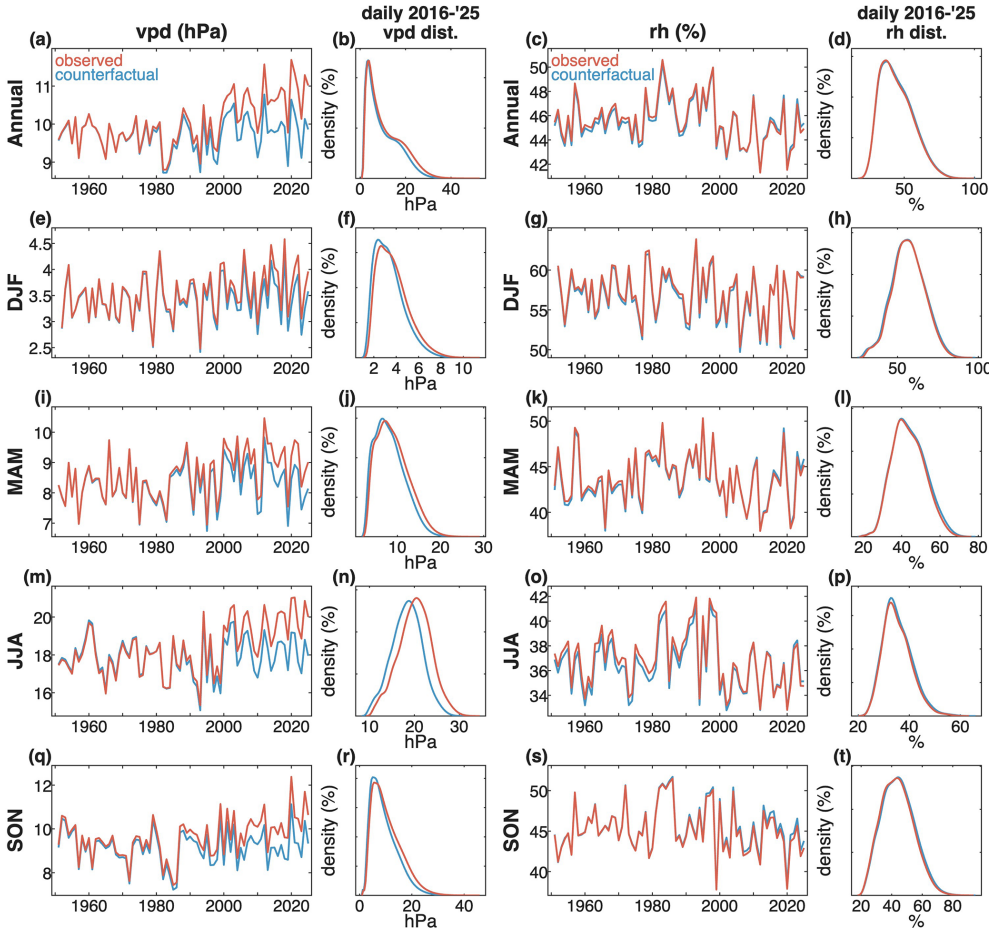

Figure A11. Observed and CMIP6-detrended vapor-pressure deficit (vpd) and relative humidity (RH) averaged across the western US. **(a, c)** Time series of mean annual vpd and RH, respectively, according to observations (orange) and the CMIP6-detrended dataset (blue). **(b, d)** Kernal density plots of daily vpd and RH, respectively, during 2016–2025. The following rows are as in **(a)**–**(d)** but for seasons (DJF: December–February, MAM: March–May, JJA: June–August, SON: September–November).

Author contributions. APW developed the methods, carried them out, and prepared the manuscript. GDM and HL helped to prepare the data. JTA, GDM, HL, SR, and CD provided critical guidance related to the methodology and edited the manuscript.

Competing interests. The contact author has declared that none of the authors has any competing interests.

Disclaimer. Publisher's note: Copernicus Publications remains neutral with regard to jurisdictional claims made in the text, published maps, institutional affiliations, or any other geographical representation in this paper. The authors bear the ultimate responsibility for providing appropriate place names. Views expressed in the text are those of the authors and do not necessarily reflect the views of the publisher.

Acknowledgements. Development of this dataset was only possible because of the careful and generous work by many individuals and organizations who are not on this author list. This includes, but is not limited to, those who established, maintained, and publicized the data from the in-situ weather stations that serve as the foundation of all of the observational data products that we used, the team that developed the NOAA nClimGrid-daily dataset (Durre et al., 2022), the team that developed the original, undownscaled ECMWF ERA5 reanalysis (Hersbach et al., 2020), individuals who contributed to the development, maintenance, and publication of the PRISM, GridMET, WTK-LED wind, WUS-D3 dynamically downscaled ERA5, and NLDAS2 gridded climate datasets; the global mean temperature datasets from NOAA, GISS, and Berkeley Earth; and the climate model simulations and associated datasets from the CMIP6. We also acknowledge the World Climate Research Programme, which, through its Working Group on Coupled Modelling, coordinated and promoted CMIP6. We thank the climate modeling groups for producing and making available their model output, the Earth System Grid Federation (ESGF) for archiving the data and

providing access, and the multiple funding agencies who support CMIP6 and ESGF.

Financial support. This research was supported by the Gordon and Betty Moore Foundation (grant no. 13283), the John Simon Guggenheim Memorial Foundation, the UCLA Sustainable LA Grand Challenge, the USGS Southwestern Climate Adaptation Science Center (grant nos. G24AC00611 and G24AC00080), and the US National Park Service (grant no. P24AC00743-00).

Review statement. This paper was edited by Martina Stockhause and reviewed by two anonymous referees.

References

Abatzoglou, J. T.: Development of gridded surface meteorological data for ecological applications and modelling, Int. J. Climatol., 33, 121–131, https://doi.org/10.1002/joc.3413, 2013.

Abatzoglou, J. T. and Williams, A. P.: Impact of anthropogenic climate change on wildfire across western US forests, P. Natl. Acad. Sci. USA, 113, 11770–11775, https://doi.org/10.1073/pnas.1607171113, 2016.

Abatzoglou, J. T., Dobrowski, S. Z., Parks, S. A., and Hegewisch, K. C.: TerraClimate, a high-resolution global dataset of monthly climate and climatic water balance from 1958–2015, Scientific Data, 5, 1–12, https://doi.org/10.1038/sdata.2017.191, 2018.

Allen, R. G., Pereira, L. S., Raes, D., and Smith, M.: Crop evapotranspiration-Guidelines for computing crop water requirements-FAO Irrigation and drainage, paper 56, Food and Agriculture Organization of the United Nations, Rome, http://www.fao.org/3/X0490E/X0490E00.htm (last access: 17 November 2026), 1998.

Anderegg, W. R. L., Anderegg, L. D. L., Kerr, K. L., and Trugman, A. T.: Widespread drought-induced tree mortality at dry range edges indicates climate stress exceeds species' compensating mechanisms, Glob. Change Biol., 25, 3793–3802, https://doi.org/10.1111/gcb.14771, 2019.

Ault, T. R., Cole, J. E., Overpeck, J. T., Pederson, G. T., and Meko, D. M.: Assessing the risk of persistent drought using climate model simulations and paleoclimate data, J. Climate, 27, 7529–7549, https://doi.org/10.1175/JCLI-D-12-00282.1, 2014.

Bellenger, H., Guilyardi, E., Leloup, J., Lengaigne, M., and Vialard, J.: ENSO representation in climate models: from CMIP3 to CMIP5, Clim. Dynam., 42, 1999–2018, https://doi.org/10.1007/s00382-013-1783-z, 2014.

Berner, L. T., Law, B. E., Meddens, A. J. H., and Hicke, J. A.: Tree mortality from fires, bark beetles, and timber harvest during a hot and dry decade in the western United States (2003–2012), Environ. Res. Lett., 12, 065005, https://doi.org/10.1088/1748-9326/aa6f94, 2017.

Bi, D., Dix, M., Marsland, S., O'farrell, S., Sullivan, A., Bodman, R., Law, R., Harman, I., Srbinovsky, J., Rashid, H. A., Dobrohotoff, P., Mackallah, C., Yan, H., Hirst, A., Savita, A., Dias, F. B., Woodhouse, M., Fiedler, R., and Heerdegen, A.: Configuration and spin-up of ACCESS-CM2, the new generation Australian community climate and earth system simulator coupled model, Journal of Southern Hemisphere Earth Systems Science, 70, 225–251, https://doi.org/10.1071/ES19040, 2020.

Brunner, L., Pendergrass, A. G., Lehner, F., Merrifield, A. L., Lorenz, R., and Knutti, R.: Reduced global warming from CMIP6 projections when weighting models by performance and independence, Earth Syst. Dynam., 11, 995–1012, https://doi.org/10.5194/esd-11-995-2020, 2020.

Byrne, H., Seager, R., and Smerdon, J. E.: CMIP6 models cannot capture long-term forced changes in the tropical Pacific sea surface temperature gradient, Nat. Commun., 17, 142, https://doi.org/10.1038/s41467-025-66839-w, 2025.

Cai, W., Santoso, A., Collins, M., Dewitte, B., Karamperidou, C., Kug, J.-S., Lengaigne, M., McPhaden, M. J., Stuecker, M. F., Taschetto, A. S., Timmermann, A., Wu, L., Yeh, S.-W., Wang, G., Ng, B., Jia, F., Yang, Y., Ying, J., Zheng, X.-T., Bayr, T., Brown, J. R., Capotondi, A., Cobb, K. M., Gan, B., Geng, T., Ham, Y.-G., Jin, F.-F., Jo, H.-S., Li, X., Lin, X., McGregor, S., Park, J.-H., Stein, K., Yang, K., Zhang, L., and Zhong, W.: Changing El Niño–Southern oscillation in a warming climate, Nat. Rev. Earth Environ., 2, 628–644, https://doi.org/10.1038/s43017-021-00199-z, 2021.

Cayan, D. R., Redmond, K. T., and Riddle, L. G.: ENSO and hydrologic extremes in the western United States, J. Climate, 12, 2881–2893, https://doi.org/10.1175/1520-0442(1999)012<2881:EAHEIT>2.0.CO;2, 1999.

Cherchi, A., Fogli, P. G., Lovato, T., Peano, D., Iovino, D., Gualdi, S., Masina, S., Scoccimarro, E., Materia, S., Bellucci, A., and Navarra, A.: Global mean climate and main patterns of variability in the CMCC-CM2 coupled model, J. Adv. Model Earth Sy., 11, 185–209, https://doi.org/10.1029/2018MS001369, 2019.

Cook, B. I., Mankin, J. S., Marvel, K., Williams, A. P., Smerdon, J. E., and Anchukaitis, K. J.: Twenty-first century drought projections in the CMIP6 forcing scenarios, Earth's Future, 8, e2019EF001461, https://doi.org/10.1029/2019EF001461, 2020.

Cox, P. M., Huntingford, C., and Williamson, M. S.: Emergent constraint on equilibrium climate sensitivity from global temperature variability, Nature, 553, 319–322, https://doi.org/10.1038/nature25450, 2018.

Daly, C., Doggett, M. K., Smith, J. I., Olson, K. V., Halbleib, M. D., Dimcovic, Z., Keon, D., Loiselle, R. A., Steinberg, B., and Ryan, A. D.: Challenges in observation-based mapping of daily precipitation across the conterminous United States, J. Atmos. Ocean. Tech., 38, 1979–1992, https://doi.org/10.1175/JTECH-D-21-0054.1, 2021.

Danabasoglu, G., Lamarque, J.-F., Bacmeister, J., Bailey, D. A., DuVivier, A. K., Edwards, J., Emmons, L. K., Fasullo, J., Garcia, R., Gettelman, A., Hannay, C., Holland, M. M., Large, W. G., Laurizen, P. H., Lawrence, D. M., Lenaerts, J. T. M., Lindsay, K., Lipscomb, W. H., Mills, M. J., Neale, R., Oleson, K. W., Otto-Bliesner, B., Phillips, A. S., Sacks, W., Tilmes, S., van Kampenhout, L., Vertenstein, M., Bertini, A., Dennis, J., Deser, C., Fischer, C., Fox-Kemper, B., Kay, J. E., Kinnison, D., Kushner, P. J., Larson, V. E., Long, M. C., Mickelson, S., Moore, J. K., Anagnostou, E. N., Polvani, L., Rasch, P. J., and Strand, W. G.: The Community Earth System Model Version 2 (CESM2), J. Adv. Model Earth Sy., 12, e2019MS001916, https://doi.org/10.1029/2019MS001916, 2020.

Dannenberg, M. P., McCabe, G. J., Wise, E. K., Johnston, M. R., Huntzinger, D. N., and Williams, A. P.: Recent increases in Mis-

souri River streamflow driven by combined effects of climate variability, land-use change, and elevated CO_2, AGU Adv., 6, e2024AV001432, https://doi.org/10.1029/2024AV001432, 2025.

Deser, C., Terray, L., and Phillips, A. S.: Forced and internal components of winter air temperature trends over North America during the past 50 years: Mechanisms and implications, J. Climate, 29, 2237–2258, https://doi.org/10.1175/JCLI-D-15-0304.1, 2016.

Dettinger, M. D., Cayan, D. R., Diaz, H. F., and Meko, D. M.: North-south precipitation patterns in western North America on interannual-to-decadal timescales, J. Climate, 11, 3095–3111, https://doi.org/10.1175/1520-0442(1998)011<3095:NSPPIW>2.0.CO;2, 1998.

Dieppois, B., Capotondi, A., Pohl, B., Chun, K. P., Monerie, P.-A., and Eden, J.: ENSO diversity shows robust decadal variations that must be captured for accurate future projections, Commun. Earth Environ., 2, 212, https://doi.org/10.1038/s43247-021-00285-6, 2021.

Diffenbaugh, N. S. and Burke, M.: Global warming has increased global economic inequality, P. Natl. Acad. Sci. USA, 116, 9808–9813, https://doi.org/10.1073/pnas.1816020116, 2019.

Döscher, R., Acosta, M., Alessandri, A., Anthoni, P., Arsouze, T., Bergman, T., Bernardello, R., Boussetta, S., Caron, L.-P., Carver, G., Castrillo, M., Catalano, F., Cvijanovic, I., Davini, P., Dekker, E., Doblas-Reyes, F. J., Docquier, D., Echevarria, P., Fladrich, U., Fuentes-Franco, R., Gröger, M., v. Hardenberg, J., Hieronymus, J., Karami, M. P., Keskinen, J.-P., Koenigk, T., Makkonen, R., Massonnet, F., Ménégoz, M., Miller, P. A., Moreno-Chamarro, E., Nieradzik, L., van Noije, T., Nolan, P., O'Donnell, D., Ollinaho, P., van den Oord, G., Ortega, P., Prims, O. T., Ramos, A., Reerink, T., Rousset, C., Ruprich-Robert, Y., Le Sager, P., Schmith, T., Schrödner, R., Serva, F., Sicardi, V., Sloth Madsen, M., Smith, B., Tian, T., Tourigny, E., Uotila, P., Vancoppenolle, M., Wang, S., Wårlind, D., Willén, U., Wyser, K., Yang, S., Yepes-Arbós, X., and Zhang, Q.: The EC-Earth3 Earth system model for the Coupled Model Intercomparison Project 6, Geosci. Model Dev., 15, 2973–3020, https://doi.org/10.5194/gmd-15-2973-2022, 2022.

Draxl, C., Wang, J., Sheridan, L., Jung, C., Bodini, N., Buckhold, S., Aghili, C. T., Peco, K., Kotamarthi, R., Kumler, A., Phillips, C., Purkayastha, A., Young, E., Rosenlieb, E., and Heidi, T.: WTK-LED: The wind toolkit long-term ensemble dataset, NREL/TP–5000-88457, National Renewable Energy Laboratory (NREL), Golden, CO, https://doi.org/10.2172/2473210, 2024.

Dunne, J. P., Horowitz, L. W., Adcroft, A. J., Ginoux, P., Held, I. M., John, J. G., Krasting, J. P., Malyshev, S., Naik, V., Paulot, F., Shevliakova, E., Stock, C. A., Zadeh, N., Balaji, V., Blanton, C., Dunne, K. A., Dupuis, C., Durachta, J., Dussin, R., Gauthier, P. P. G., Griffies, S. M., Guo, H., Hallberg, R. W., Harrison, M., He, J. H., Hurlin, W., McHugh, C., Milly, P. C. D., Nikonov, S., Paynter, D. J., Ploshay, J., Radhakrishnan, A., Rand, K., Reichl, B. G., Robinson, T., Schwarzkopf, D. M., Sentman, L. T., Underwood, S., Vahlenkamp, H., Winton, M., Wittenberg, A. T., Wyman, B., Zeng, Y., and Zhao, M.: The GFDL Earth System Model Version 4.1 (GFDL-ESM4.1): Overall coupled model description and simulation characteristics, J. Adv. Model Earth Sy., 12, e2019MS002015, https://doi.org/10.1029/2019MS002015, 2020.

Dunne, J. P., Hewitt, H. T., Arblaster, J. M., Bonou, F., Boucher, O., Cavazos, T., Dingley, B., Durack, P. J., Hassler, B., Juckes, M., Miyakawa, T., Mizielinski, M., Naik, V., Nicholls, Z., O'Rourke, E., Pincus, R., Sanderson, B. M., Simpson, I. R., and Taylor, K. E.: An evolving Coupled Model Intercomparison Project phase 7 (CMIP7) and Fast Track in support of future climate assessment, Geosci. Model Dev., 18, 6671–6700, https://doi.org/10.5194/gmd-18-6671-2025, 2025.

Durre, I., Arguez, A., Schreck III, C. J., Squires, M. F., and Vose, R. S.: Daily high-resolution temperature and precipitation fields for the contiguous United States from 1951 to present, J. Atmos. Ocean. Tech., 39, 1837–1855, https://doi.org/10.1175/JTECH-D-22-0024.1, 2022.

Eyring, V., Bony, S., Meehl, G. A., Senior, C. A., Stevens, B., Stouffer, R. J., and Taylor, K. E.: Overview of the Coupled Model Intercomparison Project Phase 6 (CMIP6) experimental design and organization, Geosci. Model Dev., 9, 1937–1958, https://doi.org/10.5194/gmd-9-1937-2016, 2016.

Eyring, V., Gillett, N. P., Achuta Rao, K. M., Barimalala, R., Barreiro Parrillo, M., Bellouin, N., Cassou, C., Durack, P. J., Kosaka, Y., McGregor, S., Min, S., Morgenstern, O., and Sun, Y.: Human influence on the climate system, chap. 3, IPCC 2021: Climate Change 2021: The Physical Science Basis. Contribution of Working Group I to the Sixth Assessment Report of the Intergovernmental Panel on Climate Change, 423–552, https://doi.org/10.1017/9781009157896.005, 2023.

Faunt, C. C., Sneed, M., Traum, J., and Brandt, J. T.: Water availability and land subsidence in the Central Valley, California, USA, Hydrogeol. J., 24, 675–684, https://doi.org/10.1007/s10040-015-1339-x, 2016.

Forster, P., Storelvmo, T., Armour, K., Collins, W., Dufresne, J.-L., Frame, D., Lunt, D. J., Mauritsen, T., Plamer, M. D., Watanabe, M., Wild, M., and Zhang, H.: The Earth's Energy Budget, Climate Feedbacks, and Climate Sensitivity, in: Climate Change 2021: The Physical Science Basis. Contribution of Working Group I to the Sixth Assessment Report of the Intergovernmental Panel on Climate Change, Cambridge University Press, Cambridge, United Kingdom and New York, NY, USA, 923–1024, https://doi.org/10.1017/9781009157896.009, 2021.

Forster, P. M., Maycock, A. C., McKenna, C. M., and Smith, C. J.: Latest climate models confirm need for urgent mitigation, Nat. Clim. Change, 10, 7–10, https://doi.org/10.1038/s41558-019-0660-0, 2020.

Gershunov, A. and Barnett, T. P.: ENSO influence on intraseasonal extreme rainfall and temperature frequencies in the contiguous United States: Observations and model results, J. Climate, 11, 1575–1586, https://doi.org/10.1175/1520-0442(1998)011<1575:EIOIER>2.0.CO;2, 1998.

Giorgi, F., Im, E.-S., Coppola, E., Diffenbaugh, N. S., Gao, X. J., Mariotti, L., and Shi, Y.: Higher hydroclimatic intensity with global warming, J. Climate, 24, 5309–5324, https://doi.org/10.1175/2011JCLI3979.1, 2011.

GISTEMP Team: GISS Surface Temperature Analysis (GISTEMP) (4), NASA Goddard Institute for Space Studies [data set], https://doi.org/10.18739/A2WW77214, 2024.

Gottlieb, A. R. and Mankin, J. S.: Evidence of human influence on Northern Hemisphere snow loss, Nature, 625, 293–300, https://doi.org/10.1038/s41586-023-06794-y, 2024.

Hajima, T., Watanabe, M., Yamamoto, A., Tatebe, H., Noguchi, M. A., Abe, M., Ohgaito, R., Ito, A., Yamazaki, D., Okajima, H., Ito, A., Takata, K., Ogochi, K., Watanabe, S., and Kawamiya, M.:

Development of the MIROC-ES2L Earth system model and the evaluation of biogeochemical processes and feedbacks, Geosci. Model Dev., 13, 2197–2244, https://doi.org/10.5194/gmd-13-2197-2020, 2020.

Hall, A. and Qu, X.: Using the current seasonal cycle to constrain snow albedo feedback in future climate change, Geophys. Res. Lett., 33, https://doi.org/10.1029/2005GL025127, 2006.

Hannart, A., Pearl, J., Otto, F. E. L., Naveau, P., and Ghil, M.: Causal counterfactual theory for the attribution of weather and climate-related events, B. Am. Meteorol. Soc., 97, 99–110, https://doi.org/10.1175/BAMS-D-14-00034.1, 2016.

Hausfather, Z., Marvel, K., Schmidt, G. A., and Nielsen-Gammon, J. W.: Climate simulations: recognize the "hot model" problem, Nature, 605, 26–29, https://doi.org/10.1038/d41586-022-01192-2, 2022.

He, C., Valayamkunnath, P., Barlage, M., Chen, F., Gochis, D., Cabell, R., Schneider, T., Rasmussen, R., Niu, G.-Y., Yang, Z.-L., Niyogi, D., and Ek, M.: Modernizing the open-source community Noah with multi-parameterization options (Noah-MP) land surface model (version 5.0) with enhanced modularity, interoperability, and applicability, Geosci. Model Dev., 16, 5131–5151, https://doi.org/10.5194/gmd-16-5131-2023, 2023.

He, Q., Williams, A. P., Johnston, M. R., Juang, C. S., and Wang, B.: Influence of time-averaging of climate data on estimates of atmospheric vapor pressure deficit and inferred relationships with wildfire area in the western United States, Geophys. Res. Lett., 52, e2024GL113708, https://doi.org/10.1029/2024GL113708, 2025.

Hersbach, H., Bell, B., Berrisford, P., Hirahara, S., Horányi, A., Muñoz-Sabater, J., Nicolas, J., Peubey, C., Radu, R., Schepers, D., Simmons, A., Soci, C., Abbdalla, S., Abellan, X., Balsamo, G., Bechtold, P., Biavati, G., Bidlot, J., Bonavita, M., De Chiara, G., Dahlgren, P., Dee, D., Diamantakis, M., Dragani, R., Flemming, J., Forbes, R., Fuentes, M., Geer, A., Haimberger, L., Healy, S., Hogan, R. J., Hólm, E., Janisková, M., Keeley, S., Laloyaux, P., Lopez, P., Lupu, C., Radnoti, R., de Rosnay, P., Rozum, I., Vamorg, F., Villaume, S., and Thêpaut, J.-N.: The ERA5 global reanalysis, Q. J. Roy. Meteor. Soc., 146, 1999–2049, https://doi.org/10.1002/qj.3803, 2020.

Hicke, J. A., Meddens, A. J. H., and Kolden, C. A.: Recent tree mortality in the western United States from bark beetles and forest fires, Forest Sci., 62, 141–153, https://doi.org/10.5849/forsci.15-086, 2016.

Hirsch, A. L., Ridder, N. N., Perkins-Kirkpatrick, S. E., and Ukkola, A.: CMIP6 MultiModel evaluation of present-day heatwave attributes, Geophys. Res. Lett., 48, e2021GL095161, https://doi.org/10.1029/2021GL095161, 2021.

Howitt, R., Medellin-Azuara, J., MacEwan, D., Lund, J., and Sumner, D. A.: Economic analysis of the 2014 drought for California agriculture, UC Davis Center for Watershed Sciences, Davis, CA, https://watershed.ucdavis.edu/sites/g/files/dgvnsk8531/files/products/2021-05/DroughtReport_23July2014_0.pdf (last access: 20 November 2026), 2014.

Hu, G. and Franzke, C. L. E.: Evaluation of daily precipitation extremes in reanalysis and gridded observation-based data sets over Germany, Geophys. Res. Lett., 47, e2020GL089624, https://doi.org/10.1029/2020GL089624, 2020.

Huang, B., Yin, X., Menne, M. J., and Vose, R.: NOAA Global Surface Temperature Dataset (NOAAGlobalTemp) (6.1.0), NOAA National Centers for Environmental Information [data set], https://doi.org/10.25921/vvaa-wq11, 2026.

Hung, M. J. and Williams, A. P.: High-severity fire now dominant in California forests, P. Natl. Acad. Sci. USA, 123, e2532829123, https://doi.org/10.1073/pnas.2532829123, 2026.

Jiang, F., Seager, R., and Cane, M. A.: Historical subsurface cooling in the tropical Pacific and its dynamics, J. Climate, 37, 5925–5938, https://doi.org/10.1175/JCLI-D-24-0007.1, 2024.

Jiang, F., Seager, R., Cane, M. A., Karamperidou, C., and Brizuela, N. G.: Subsurface cooling and sea surface temperature pattern formation over the equatorial Pacific, J. Geophys. Res.-Oceans, 130, e2024JC022222, https://doi.org/10.1029/2024JC022222, 2025.

Juang, C. S., Williams, A. P., Abazoglou, J. T., Balch, J. K., Hurteau, M. D., and Moritz, M. A.: Rapid growth of large forest fires drives the exponential response of annual forest-fire area to aridity in the western United States, Geophys. Res. Lett., 49, e2021GL097131, https://doi.org/10.1029/2021GL097131, 2022.

Knutti, R., Sedláček, J., Sanderson, B. M., Lorenz, R., Fischer, E. M., and Eyring, V.: A climate model projection weighting scheme accounting for performance and interdependence, Geophys. Res. Lett., 44, 1909–1918, https://doi.org/10.1002/2016GL072012, 2017a.

Knutti, R., Rugenstein, M. A. A., and Hegerl, G. C.: Beyond equilibrium climate sensitivity, Nat. Geosci., 10, 727–736, https://doi.org/10.1038/ngeo3017, 2017b.

Koszuta, M., Siler, N., Leung, L. R., and Wettstein, J. J.: Weakened orographic influence on cool-season precipitation in simulations of future warming over the western US, Geophys. Res. Lett., 51, e2023GL107298, https://doi.org/10.1029/2023GL107298, 2024.

Krantz, W., Pierce, D., Goldenson, N., and Cayan, D.: Memorandum on Evaluating Global Climate Models for Studying Regional Climate Change in California, California Energy Commission's applied research grant EPC-20-006: Development of Climate Projections for California and Identification of Priority Projections, EPC-20-006, California Energy Commission, Scripps Institution of Oceanography, https://www.energy.ca.gov/sites/default/files/2022-09/20220907_CDAWG_MemoEvaluating_GCMs_EPC-20-006_Nov2021-ADA.pdf (last access: 17 November 2026), 2022.

Lee, J., Kim, J., Sun, M.-A., Kim, B.-H., Moon, H., Sung, H. M., Kim, J., and Byun, Y.-H.: Evaluation of the Korea Meteorological Administration Advanced Community Earth-System model (K-ACE), Asia-Pac. J. Atmos. Sci., 56, 381–395, https://doi.org/10.1007/s13143-019-00144-7, 2020.

Lehner, F., Deser, C., Simpson, I. R., and Terray, L.: Attributing the US Southwest's recent shift into drier conditions, Geophys. Res. Lett., 45, 6251–6261, https://doi.org/10.1029/2018GL078312, 2018.

Letcher, T. W. and Minder, J. R.: Characterization of the simulated regional snow albedo feedback using a regional climate model over complex terrain, J. Climate, 28, 7576–7595, https://doi.org/10.1175/JCLI-D-15-0166.1, 2015.

Li, L., Yu, Y., Tang, Y., Lin, P., Xie, J., Song, M., Dong, L., Zhou, T., Liu, L., Wang, L., Pu, Y., Chen, X., Chen, L., Xie, Z., Liu, H., Zhang, L., Huang, X., Feng, T., Zheng, W., Xia, K., Liu, H., Liu, J., Wang, Y., Wang, L., Jia, B., Xia, F., Wang, B., Zhao, S., Yu, Z., Zhao, B., and Wei, J.: The Flexible Global Ocean-Atmosphere-Land System

Model Grid-Point version 3 (FGOALS-g3): Description and evaluation, J. Adv. Model. Earth Sy., 12, e2019MS002012, https://doi.org/10.1029/2019MS002012, 2020.

Li, Z. and Ding, Q.: A global poleward shift of atmospheric rivers, Sci. Adv., 10, eadq0604, https://doi.org/10.1126/sciadv.adq0604, 2024.

Liang, Y., Gillett, N. P., and Monahan, A. H.: Climate model projections of 21st century global warming constrained using the observed warming trend, Geophys. Res. Lett., 47, e2019GL086757, https://doi.org/10.1029/2019GL086757, 2020.

Lorenz, R., Herger, N., Sedláček, J., Eyring, V., Fischer, E. M., and Knutti, R.: Prospects and caveats of weighting climate models for summer maximum temperature projections over North America, J. Geophys. Res.-Atmos., 123, 4509–4526, https://doi.org/10.1029/2017JD027992, 2018.

Madakumbura, G. D., Abolafia-Rosenzweig, R., He, C., Jones, J., He, Q., Revel, M., Wang, B., and Williams, A. P.: A 4-km long-term (1952–2025) daily hydrometeorological dataset for the western United States, Scientific Data, 13, 1418, https://doi.org/10.1038/s41597-026-07642-0, 2026.

Marvel, K. and Bonfils, C.: Identifying external influences on global precipitation, P. Natl. Acad. Sci. USA, 110, 19301–19306, https://doi.org/10.1073/pnas.1314382110, 2013.

Mauritsen, T., Bader, J., Becker, T., Behrens, J., Bittner, M., Brokopf, R., Brovkin, V., Claussen, M., Crueger, T., and Esch, M.: Developments in the MPI-M Earth System Model version 1.2 (MPI-ESM1. 2) and its response to increasing CO_2, J. Adv. Model Earth Sy., 11, 998–1038, https://doi.org/10.1029/2018MS001400, 2019.

McCabe, G. J. and Dettinger, M. D.: Decadal variations in the strength of ENSO teleconnections with precipitation in the western United States, Int. J. Climatol., 19, 1399–1410, https://doi.org/10.1002/(SICI)1097-0088(19991115)19:13%3C1399::AID-JOC457%3E3.0.CO;2-A, 1999.

McCrary, R. R., Mearns, L. O., Abel, M. R., Biner, S., and Bukovsky, M. S.: Projections of North American snow from NA-CORDEX and their uncertainties, with a focus on model resolution, Climatic Change, 170, 20, https://doi.org/10.1007/s10584-021-03294-8, 2022.

Meinshausen, M., Nicholls, Z. R. J., Lewis, J., Gidden, M. J., Vogel, E., Freund, M., Beyerle, U., Gessner, C., Nauels, A., Bauer, N., Canadell, J. G., Daniel, J. S., John, A., Krummel, P. B., Luderer, G., Meinshausen, N., Montzka, S. A., Rayner, P. J., Reimann, S., Smith, S. J., van den Berg, M., Velders, G. J. M., Vollmer, M. K., and Wang, R. H. J.: The shared socioeconomic pathway (SSP) greenhouse gas concentrations and their extensions to 2500, Geosci. Model Dev., 13, 3571–3605, https://doi.org/10.5194/gmd-13-3571-2020, 2020.

Mengel, M., Treu, S., Lange, S., and Frieler, K.: ATTRICI v1.1 – counterfactual climate for impact attribution, Geosci. Model Dev., 14, 5269–5284, https://doi.org/10.5194/gmd-14-5269-2021, 2021.

Merrifield, A. L., Brunner, L., Lorenz, R., Medhaug, I., and Knutti, R.: An investigation of weighting schemes suitable for incorporating large ensembles into multi-model ensembles, Earth Syst. Dynam., 11, 807–834, https://doi.org/10.5194/esd-11-807-2020, 2020.

Mote, P. W., Li, S., Lettenmaier, D. P., Xiao, M., and Engel, R.: Dramatic declines in snowpack in the western US, npj Climate Atmos. Sci., 1, https://doi.org/10.1038/s41612-018-0012-1, 2018.

Musselman, K. N., Addor, N., Vano, J. A., and Molotch, N. P.: Winter melt trends portend widespread declines in snow water resources, Nat. Clim. Change, 11, 418–424, https://doi.org/10.1038/s41558-021-01014-9, 2021.

National Academies of Sciences, Engineering, and Medicine: Attribution of Extreme Weather Events in the Context of Climate Change, The National Academies Press, Washington, D. C., 166 pp., https://doi.org/10.17226/21852, 2016.

Newman, M., Alexander, M. A., Ault, T. R., Cobb, K. M., Deser, C., Di Lorenzo, E., Mantua, N. J., Miller, A. J., Minobe, S., Nakamura, H., Schneider, N., Vimont, D. J., Phillips, A. S., scott, J. S., and Smith, C. A.: The Pacific Decadal Oscillation, revisited, J. Climate, 29, 4399–4427, https://doi.org/10.1175/JCLI-D-15-0508.1, 2016.

Nijsse, F. J. M. M., Cox, P. M., and Williamson, M. S.: Emergent constraints on transient climate response (TCR) and equilibrium climate sensitivity (ECS) from historical warming in CMIP5 and CMIP6 models, Earth Syst. Dynam., 11, 737–750, https://doi.org/10.5194/esd-11-737-2020, 2020.

NOAA: US Standard Atmosphere, 1976, NOAA-S/T 76-1562, National Oceanic and Atmospheric Administration, Washington, D. C., https://ntrs.nasa.gov/citations/19770009539 (last access: 17 November 2026), 1976.

Noyelle, R., Wills, R. J., Fischer, E., Wernli, H., and Knutti, R.: Climate models lack decadal variability in precipitation because of a weak atmospheric response to sea surface temperature anomalies, EGUsphere [preprint], https://doi.org/10.5194/egusphere-2026-6524, 2026.

O'Neill, B. C., Tebaldi, C., van Vuuren, D. P., Eyring, V., Friedlingstein, P., Hurtt, G., Knutti, R., Kriegler, E., Lamarque, J.-F., Lowe, J., Meehl, G. A., Moss, R., Riahi, K., and Sanderson, B. M.: The Scenario Model Intercomparison Project (ScenarioMIP) for CMIP6, Geosci. Model Dev., 9, 3461–3482, https://doi.org/10.5194/gmd-9-3461-2016, 2016.

Parks, S. A., Coop, J. D., and Davis, K. T.: Intensifying Fire Season Aridity Portends Ongoing Expansion of Severe Wildfire in Western US Forests, Glob. Change Biol., 31, e70429, https://doi.org/10.1111/gcb.70429, 2025.

Payne, A. E. and Magnusdottir, G.: An evaluation of atmospheric rivers over the North Pacific in CMIP5 and their response to warming under RCP 8.5, J. Geophys. Res.-Atmos., 120, 11–173, https://doi.org/10.1002/2015JD023586, 2015.

Peco, K., Wang, J., Jung, C., Sever, G., Sheridan, L., Feinstein, J., Kotamarthi, R., Draxl, C., Young, E., Purkayastha, A., and Kumler, A.: Evaluation of a high-resolution regional climate simulation for surface and hub-height wind climatology over North America, Wind Energ. Sci., 11, 13–35, https://doi.org/10.5194/wes-11-13-2026, 2026.

Pendergrass, A. G., Knutti, R., Lehner, F., Deser, C., and Sanderson, B. M.: Precipitation variability increases in a warmer climate, Sci. Rep., 7, 17966, https://doi.org/10.1038/s41598-017-17966-y, 2017.

Pepin, N., Apple, M., Knowles, J., Terzago, S., Arnone, E., Hänchen, L., Napoli, A., Potter, E., Steiner, J., Williamson, S. N., Williamson, S. N., Ahrens, B., Dhar, T., Dimri, A. P., Palazzi, E., Rameshan, A., Salzmann, N., Shahgedanova, M., de Deous Vi-

dal Jr., J., and Zardi, D.: Elevation-dependent climate change in mountain environments, Nature Reviews Earth & Environment, 6, 772–788, https://doi.org/10.1038/s43017-025-00740-4, 2025.

Pfahl, S., O'Gorman, P. A., and Fischer, E. M.: Understanding the regional pattern of projected future changes in extreme precipitation, Nat. Clim. Change, 7, 423–427, https://doi.org/10.1038/nclimate3287, 2017.

Pierce, D. W., Cayan, D. R., Goodrich, J., Das, T., and Munévar, A.: Evaluating global climate models for hydrological studies of the upper Colorado River Basin, J. Am. Water Resour. As., 58, 709–734, https://doi.org/10.1111/1752-1688.12974, 2022.

Pillai, J. R., Armour, K. C., and Battisti, D. S.: The Influence of Historical Sea Surface Temperature Patterns on Regional Precipitation Trends, J. Climate, 39, 2333–2349, https://doi.org/10.1175/JCLI-D-25-0446.1, 2026.

Planton, Y. Y., Guilyardi, E., Wittenberg, A. T., Lee, J., Gleckler, P. J., Bayr, T., McGregor, S., McPhaden, M. J., Power, S., Roehrig, R., Vialard, J., and Voldoire, A.: Evaluating climate models with the CLIVAR 2020 ENSO metrics package, B. Am. Meteorol. Soc., 102, E193–E217, https://doi.org/10.1175/BAMS-D-19-0337.1, 2021.

Rahimi, S., Krantz, W., Lin, Y.-H., Bass, B., Goldenson, N., Hall, A., Lebo, Z. J., and Norris, J.: Evaluation of a Reanalysis-Driven Configuration of WRF4 Over the Western United States From 1980 to 2020, J. Geophys. Res.-Atmos., 127, e2021JD035699, https://doi.org/10.1029/2021JD035699, 2022.

Rahimi, S., Huang, L., Norris, J., Hall, A., Goldenson, N., Krantz, W., Bass, B., Thackeray, C., Lin, H., Chen, D., Dennis, E., Collins, E., Lebo, Z. J., Slinskey, E., Graves, S., Biyani, S., Wang, B., Cropper, S., and the UCLA Center for Climate Science Team: An overview of the Western United States Dynamically Downscaled Dataset (WUS-D3), Geosci. Model Dev., 17, 2265–2286, https://doi.org/10.5194/gmd-17-2265-2024, 2024.

Ribes, A., Qasmi, S., and Gillett, N. P.: Making climate projections conditional on historical observations, Science Advances, 7, eabc0671, https://doi.org/10.1126/sciadv.abc0671, 2021.

Rodell, M., Famiglietti, J. S., Wiese, D. N., Reager, J. T., Beaudoing, H. K., Landerer, F. W., and Lo, M.-H.: Emerging trends in global freshwater availability, Nature, 557, 651–659, https://doi.org/10.1038/s41586-018-0123-1, 2018.

Rohde, R. A. and Hausfather, Z.: The Berkeley Earth Land/Ocean Temperature Record, Earth Syst. Sci. Data, 12, 3469–3479, https://doi.org/10.5194/essd-12-3469-2020, 2020.

Ropelewski, C. F. and Halpert, M. S.: North American precipitation and temperature patterns associated with the El Niño/Southern Oscillation (ENSO), Mon. Weather Rev., 114, 2352–2362, https://doi.org/10.1175/1520-0493(1986)114%3C2352:NAPATP%3E2.0.CO;2, 1986.

Rupp, D. E., Daly, C., Doggett, M. K., Smith, J. I., and Steinberg, B.: Mapping an observation-based global solar irradiance climatology across the conterminous United States, J. Appl. Meteorol. Clim., 61, 857–876, https://doi.org/10.1175/JAMC-D-21-0236.1, 2022.

Sanderson, B. M., Knutti, R., and Caldwell, P.: A representative democracy to reduce interdependency in a multimodel ensemble, J. Climate, 28, 5171–5194, https://doi.org/10.1175/JCLI-D-14-00362.1, 2015.

Sanderson, B. M., Wehner, M., and Knutti, R.: Skill and independence weighting for multi-model assessments, Geosci. Model Dev., 10, 2379–2395, https://doi.org/10.5194/gmd-10-2379-2017, 2017.

Schwalm, C. R., Williams, C. A., Schaefer, K., Baldocchi, D., Black, T. A., Goldstein, A. H., Law, B. E., Oechel, W. C., U, K. T. P., and Scott, R. L.: Reduction in carbon uptake during turn of the century drought in western North America, Nat. Geosci., 5, 551–556, https://doi.org/10.1038/ngeo1529, 2012.

Seager, R., Cane, M., Henderson, N., Lee, D.-E., Abernathy, R., and Zhang, H.: Strengthening tropical Pacific zonal sea surface temperature gradient consistent with greenhouse gases, Nat. Clim. Change, 9, 517–522, https://doi.org/10.1038/s41558-019-0505-x, 2019.

Seager, R., Henderson, N., and Cane, M.: Persistent discrepancies between observed and modeled trends in the tropical Pacific Ocean, J. Climate, 35, 4571–4584, https://doi.org/10.1175/JCLI-D-21-0648.1, 2022.

Seager, R., Ting, M., Alexander, P., Liu, H., Nakamura, J., Li, C., and Newman, M.: Ocean-forcing of cool season precipitation drives ongoing and future decadal drought in southwestern North America, npj Climate and Atmospheric Science, 6, 141, https://doi.org/10.1038/s41612-023-00461-9, 2023.

Séférian, R., Nabat, P., Michou, M., Saint-Martin, D., Voldoire, A., Colin, J., Decharme, B., Delire, C., Berthet, S., and Chevallier, M.: Evaluation of CNRM Earth system model, CNRM-ESM2-1: Role of Earth system processes in present-day and future climate, J. Adv. Model. Earth Sy., 11, 4182–4227, https://doi.org/10.1029/2019MS001791, 2019.

Seland, Ø., Bentsen, M., Olivié, D., Toniazzo, T., Gjermundsen, A., Graff, L. S., Debernard, J. B., Gupta, A. K., He, Y.-C., Kirkevåg, A., Schwinger, J., Tjiputra, J., Aas, K. S., Bethke, I., Fan, Y., Griesfeller, J., Grini, A., Guo, C., Ilicak, M., Karset, I. H. H., Landgren, O., Liakka, J., Moseid, K. O., Nummelin, A., Spensberger, C., Tang, H., Zhang, Z., Heinze, C., Iversen, T., and Schulz, M.: Overview of the Norwegian Earth System Model (NorESM2) and key climate response of CMIP6 DECK, historical, and scenario simulations, Geosci. Model Dev., 13, 6165–6200, https://doi.org/10.5194/gmd-13-6165-2020, 2020.

Sellar, A. A., Jones, C. G., Mulcahy, J. P., Tang, Y., Yool, A., Wiltshire, A., O'Connor, F. M., Stringer, M., Hill, R., Palmieri, J., Woodward, S., de Mora, L., Kuhlbrodt, T., Rumbold, S. T., Kelley, M., Ellis, R., Johnson, C. E., Walton, J., Abraham, N. L., Andrews, M. B., Andrews, T., Archibald, A. T., Berthou, S., Burke, E., Blockley, E., Carslaw, K., Dalvi, M., Edwards, J., Folberth, G. A., Gedney, N., Griffiths, P. T., Harper, A. B., Hendry, M. A., Hewitt, H. T., Johnson, B., Jones, A., Jones, C. D., Keeble, J., Liddicoat, S., Morgenstern, O., Parker, R. J., Predoi, V., Robertson, E., Siahaan, A., Smith, R. S., Swaminathan, R., Woodhouse, M. T., Zeng, G., and Zerroukat, M.: UKESM1: Description and evaluation of the U.K. Earth System Model, J. Adv. Model. Earth Sy., 11, 4513–4558, https://doi.org/10.1029/2019MS001739, 2019.

Siler, N. and Roe, G.: How will orographic precipitation respond to surface warming? An idealized thermodynamic perspective, Geophys. Res. Lett., 41, 2606–2613, https://doi.org/10.1002/2013GL059095, 2014.

Sippel, S., Meinshausen, N., Fischer, E. M., Székely, E., and Knutti, R.: Climate change now detectable from any single day of weather at global scale, Nat. Clim. Change, 10, 35–41, https://doi.org/10.1038/s41558-019-0666-7, 2020.

Smith, E., Grant, N., Luo, X., and Diaz, D.: Evaluating the ability of gridded climate datasets to capture temperature and precipitation trends and extremes, Sci. Rep., 15, 12607, https://doi.org/10.1038/s41598-025-97570-7, 2025.

Stephens, S. L., Steel, Z. L., Collins, B. M., Fry, D. L., Gill, S. J., Rivera-Huerta, H., and Skinner, C. N.: Climate and fire impacts on tree recruitment in mixed conifer forests in northwestern Mexico and California, Ecol. Appl., 33, e2844, https://doi.org/10.1002/eap.2844, 2023.

Sun, Q., Miao, C., Duan, Q., Ashouri, H., Sorooshian, S., and Hsu, K.-L.: A review of global precipitation data sets: Data sources, estimation, and intercomparisons, Rev. Geophys., 56, 79–107, https://doi.org/10.1002/2017RG000574, 2018.

Swain, D. L., Prein, A. F., Abatzoglou, J. T., Albano, C. M., Brunner, M., Diffenbaugh, N. S., Singh, D., Skinner, C. B., and Touma, D.: Hydroclimate volatility on a warming Earth, Nat. Rev. Earth Environ., 6, 35–50, https://doi.org/10.1038/s43017-024-00624-z, 2025.

Swart, N. C., Cole, J. N. S., Kharin, V. V., Lazare, M., Scinocca, J. F., Gillett, N. P., Anstey, J., Arora, V., Christian, J. R., Hanna, S., Jiao, Y., Lee, W. G., Majaess, F., Saenko, O. A., Seiler, C., Seinen, C., Shao, A., Sigmond, M., Solheim, L., von Salzen, K., Yang, D., and Winter, B.: The Canadian Earth System Model version 5 (CanESM5.0.3), Geosci. Model Dev., 12, 4823–4873, https://doi.org/10.5194/gmd-12-4823-2019, 2019.

Tatebe, H., Ogura, T., Nitta, T., Komuro, Y., Ogochi, K., Takemura, T., Sudo, K., Sekiguchi, M., Abe, M., Saito, F., Chikira, M., Watanabe, S., Mori, M., Hirota, N., Kawatani, Y., Mochizuki, T., Yoshimura, K., Takata, K., O'ishi, R., Yamazaki, D., Suzuki, T., Kurogi, M., Kataoka, T., Watanabe, M., and Kimoto, M.: Description and basic evaluation of simulated mean state, internal variability, and climate sensitivity in MIROC6, Geosci. Model Dev., 12, 2727–2765, https://doi.org/10.5194/gmd-12-2727-2019, 2019.

Taylor, K. E., Stouffer, R. J., and Meehl, G. A.: An overview of CMIP5 and the experiment design, B. Am. Meteorol. Soc., 93, 485–498, https://doi.org/10.1175/BAMS-D-11-00094.1, 2012.

Tokarska, K. B., Stolpe, M. B., Sippel, S., Fischer, E. M., Smith, C. J., Lehner, F., and Knutti, R.: Past warming trend constrains future warming in CMIP6 models, Sci. Adv., 6, eaaz9549, https://doi.org/10.1126/sciadv.aaz9549, 2020.

Voldoire, A., Saint-Martin, D., Sénési, S., Decharme, B., Alias, A., Chevallier, M., Colin, J., Guérémy, J.-F., Michou, M., Moine, M.-P., Nabat, P., Roehrig, R., Salas y Mélia, D., Séférian, R., Valcke, S., Beau, I., Belamari, S., Berthet, S., Cassou, C., Cattiaux, J., Deshayes, J., Douville, H., Ethé, C., Franchistéguy, L., Geoffroy, O., Lévy, C., Madec, G., Meurdesoif, Y., Msadek, R., Ribes, A., Sanchez-Gomez, E., and Waldman, R.: Evaluation of CMIP6 DECK Experiments With CNRM-CM6-1, J. Adv. Model. Earth Sy., 11, 2177–2213, https://doi.org/10.1029/2019MS001683, 2019.

Volodin, E. M., Mortikov, E. V., Kostrykin, S. V., Galin, V. Y., Lykossov, V. N., Gritsun, A. S., Diansky, N. A., Gusev, A. V., Iakovlev, N. G., Shestakova, A. A., and Emelina, S. V.: Simulation of the modern climate using the INM-CM4-8 model, Russ. J. Numer. Anal. M., 33, 367–374, https://doi.org/10.1515/rnam-2018-0032, 2017.

Volodin, E. M., Mortikov, E. V., Kostrykin, S. V., Galin, V. Y., Lykossov, V. N., Gritsun, A. S., Diansky, N. A., Gusev, A. V., and Iakovlev, N. G.: Simulation of the present-day climate with the INMCM5 model, Clim. Dynam., 49, 3715–3734, https://doi.org/10.1007/s00382-017-3539-7, 2018.

Wang, J., Bodini, N., Purkayastha, A., Young, E., and Draxl, C.: WIND Toolkit Long-Term Ensemble Dataset, Open Energy Data Initiative (OEDI), National Renewable Energy Laboratory (NREL) [data set], https://doi.org/10.25984/2504176, 2024.

Williams, A. P.: Code and data resources to remove CMIP6 anthropogenic trends from western US daily observed climate (1.0), Zenodo [code], https://doi.org/10.5281/zenodo.20345319, 2026a.

Williams, A. P.: Couterfactual version of 1/24-degree gridded daily observed climate for the western United States after removal of CMIP6 trends in background means and daily variances, 1951–2025, Zenodo [data set], https://doi.org/10.5281/zenodo.20261472, 2026b.

Williams, A. P.: Gridded 1/24-degree daily climate for the western United States, 1951–2025 (1.0), Zenodo [data set], https://doi.org/10.5281/zenodo.24118479, 2026c.

Williams, A. P., Allen, C. D., Macalady, A. K., Griffin, D., Woodhouse, C. A., Meko, D. M., Swetnam, T. W., Rauscher, S. A., Seager, R., Grissino Mayer, H. D., Dean, J. S., Cook, E. R., Gangodagamage, C., Cai, M., and McDowell, N. G.: Temperature as a potent driver of regional forest drought stress and tree mortality, Nat. Clim. Change, 3, 292–297, https://doi.org/10.1038/nclimate1693, 2013.

Williams, A. P., Seager, R., Abatzoglou, J. T., Cook, B. I., Smerdon, J. E., and Cook, E. R.: Contribution of anthropogenic warming to California drought during 2012–2014, Geophys. Res. Lett., 42, 6819–6828, https://doi.org/10.1002/2015GL064924, 2015.

Williams, A. P., Cook, E. R., Smerdon, J. E., Cook, B. I., Abatzoglou, J. T., Bolles, K., Baek, S. H., Badger, A., and Livneh, B.: Large contribution from anthropogenic warming to a developing North American megadrought, Science, 368, 314–318, https://doi.org/10.1126/science.aaz9600, 2020.

Williams, A. P., Livneh, B., McKinnon, K. A., Hansen, W. D., Mankin, J. S., Cook, B. I., Smerdon, J. E., Varuolo-Clarke, A. M., Bjarke, N. R., and Juang, C. S.: Growing impact of wildfire on western US water supply, P. Natl. Acad. Sci. USA, 119, e2114069119, https://doi.org/10.1073/pnas.2114069119, 2022a.

Williams, A. P., Cook, B. I., and Smerdon, J. E.: Rapid intensification of the emerging southwestern North American megadrought in 2020–2021, Nat. Clim. Change, 12, 232–234, https://doi.org/10.1038/s41558-022-01290-z, 2022b.

Williams, A. P., McKinnon, K. A., Anchukaitis, K. J., Gershunov, A., Varuolo-Clarke, A. M., Clemesha, R. E., and Liu, H.: Anthropogenic intensification of cool-season precipitation is not yet detectable across the western United States, J. Geophys. Res.-Atmos., 129, e2023JD040537, https://doi.org/10.1029/2023JD040537, 2024a.

Williams, D. N., Balaji, V., Cinquini, L., Denvil, S., Duffy, D., Evans, B., Ferraro, R., Hansen, R., Lautenschlager, M., and Trenham, C.: A global repository for planet-sized experiments and observations, B. Am. Meteorol. Soc., 97, 803–816, https://doi.org/10.1175/BAMS-D-15-00132.1, 2016.

Williams, E. L. and Abatzoglou, J. T.: Climate change increases evaporative and crop irrigation demand in North America, Earth's Future, 13, e2025EF005931, https://doi.org/10.1029/2025EF005931, 2025.

Williams, E. L., Abatzoglou, J. T., Hegewisch, K. C., and Williams, A. P.: Anthropogenic climate change has reduced drought recovery probabilities across the western US, Communications Earth & Environment, 5, 546, https://doi.org/10.1038/s43247-024-01640-z, 2024b.

Williams, K. D., Copsey, D., Blockley, E. W., Bodas-Salcedo, A., Calvert, D., Comer, R., Davis, P., Graham, T., Hewitt, H. T., Hill, R., Hyder, P., Ineson, S., Johns, T. C., Keen, A. B., Lee, R. W., Megann, A., Milton, S. F., Rae, L. G. L., Roberts, M. J., Scaife, A. A., Schiemann, R., Storkey, D., Thorpe, L., Watterson, I. G., Walters, D. N., West, A., Wood, R. A., Woolings, T., and Xavier, P. K.: The Met Office Global Coupled Model 3.0 and 3.1 (GC3.0 and GC3.1) configurations, J. Adv. Model. Earth Sy., 10, 357–380, https://doi.org/10.1002/2017MS001115, 2018.

WMO: Guide to Meteorological Instruments and Methods of Observation, WMO-No. 8, World Meteorological Organization, Geneva, Switzerland, https://wmo.int/guide-instruments-and-methods-of-observation-wmo-no-8-0 (last access: 17 November 2026), 2008.

WMO: The State of Greenhouse Gases in the Atmosphere Based on Global Observations through 2025, WMO Greenhouse Gas Bulletin, 22, World Meteorological Organization, Geneva, https://library.wmo.int/idurl/4/69986 (last access: 17 November 2026), 2026.

Xia, Y., Mitchell, K., Ek, M., Sheffield, J., Cosgrove, B., Wood, E., Luo, L., Alonge, C., Wei, H., Meng, J., Linvneh, B., Lettenmaier, D., Koren, V., Duan, Q., Mo, K., Fan, Y., and Mocko, D.: Continental-scale water and energy flux analysis and validation for the North American Land Data Assimilation System project phase 2 (NLDAS-2): 1. Intercomparison and application of model products, J. Geophys. Res.-Atmos., 117, D03109, https://doi.org/10.1029/2011JD016051, 2012.

Xiao, M., Udall, B., and Lettenmaier, D. P.: On the causes of declining Colorado River streamflows, Water Resour. Res., 54, 6739–6756, https://doi.org/10.1029/2018WR023153, 2018.

Yukimoto, S., Kawai, H., Koshiro, T., Oshima, N., Yoshida, K., Urakawa, S., Tsujino, H., Deushi, M., Tanaka, T., Hosaka, M., Yabu, S., Yoshimura, H., Shindo, E., Mizuta, R., Obata, A., Adachi, Y., and Ishii, M.: The Meteorological Research Institute Earth System Model Version 2.0, MRI-ESM2.0: Description and basic evaluation of the physical component, J. Meteorol. Soc. Jpn. Ser. II, 97, 931–965, https://doi.org/10.2151/jmsj.2019-051, 2019.

Zelinka, M. D., Myers, T. A., McCoy, D. T., Po-Chedley, S., Caldwell, P. M., Ceppi, P., Klein, S. A., and Taylor, K. E.: Causes of higher climate sensitivity in CMIP6 models, Geophys. Res. Lett., 47, e2019GL085782, https://doi.org/10.1029/2019GL085782, 2020.

Zhang, W., Furtado, K., Wu, P., Zhou, T., Chadwick, R., Marzin, C., Rostron, J., and Sexton, D.: Increasing precipitation variability on daily-to-multiyear time scales in a warmer world, Science Advances, 7, eabf8021, https://doi.org/10.1126/sciadv.abf8021, 2021.

Zhu, J., Poulsen, C. J., and Otto-Bliesner, B. L.: High climate sensitivity in CMIP6 model not supported by paleoclimate, Nat. Clim. Change, 10, 378–379, https://doi.org/10.1038/s41558-020-0764-6, 2020.

Ziehn, T., Chamberlain, M. A., Law, R. M., Lenton, A., Bodman, R. W., Dix, M., Stevens, M., Wang, Y.-P., and Srbinovsky, J.: The Australian Earth System Model: ACCESS-ESM1.5, Journal of Southern Hemisphere Earth Systems Science, 70, 193–214, https://doi.org/10.1071/ES19035, 2020.